Science of the Total Environment 992 (2025) 179922

Contents lists available at ScienceDirect

Science of the Total Environment

journal homepage: www.elsevier.com/locate/scitotenv

Human-induced carbon stress power upon earth: integrated data set, rheological findings and consequences

Matthias Jonas[a,*], Rostyslav Bun[b,c], Iryna Ryzha[b], Piotr Żebrowski[a]

[a] Advancing Systems Analysis Program, International Institute for Applied Systems Analysis, 2361 Laxenburg, Austria
[b] Department of Applied Mathematics, Lviv Polytechnic National University, 79013 Lviv, Ukraine
[c] Department of Transport and Computer Sciences, WSB University, 41300 Dąbrowa Górnicza, Poland

HIGHLIGHTS

- Anthropogenic emissions of CO_2 are perceived as stressor upon Earth.
- Earth's stress–strain (rheological) balance is quantified for the first time.
- Human stress power increased globally during 1850–2021 from 0 to ~15$Payr^{-1}$.
- Earth's strain response increased during 1850–2021 from 0 to ~24.
- Earth's uptake of carbon increased until ~1932 and decreased markedly since then.

GRAPHICAL ABSTRACT

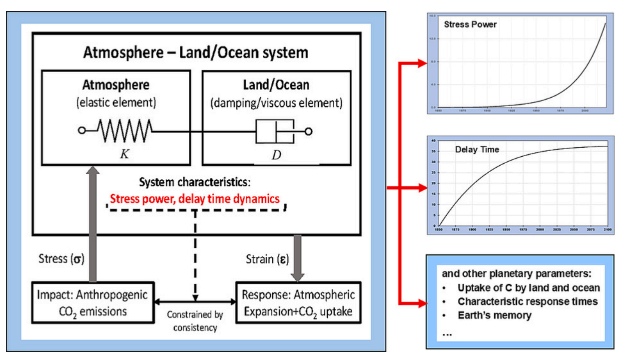

ARTICLE INFO

Editor: Philip Hopke

Keywords:
System Earth
Atmosphere and land-ocean carbon system
Human-induced carbon emissions
Stress power upon Earth
Earth's strain response
Earth's rheological parameters

ABSTRACT

In this study we take the position of an outer-space observer to understand Earth's planetary carbon-climate response to stress from a rheological perspective; with stress upon the Earth atmosphere–land and ocean system given by the uninterrupted increase in cumulative CO_2 emissions caused by humankind between 1850 and 2021. This perspective complements the global carbon mass balance perspective applied by the carbon community. It gives reason to suspect that Earth is in an even worse environmental condition than commonly believed.

We apply a rheological (stress–strain) analogue model, a Maxwell body, consisting of elastic and damping (viscous) elements to reflect the overall behavior of the atmosphere–land and ocean system under the influence of global warming. For an observer it is the overall strain response of that system – expansion of the atmosphere by volume and uptake of CO_2 by sinks – that is unknown.

Our rheological study addresses two important issues that had neither been mentioned previously nor elsewhere. Firstly, we quantify stress power exerted by humans upon Earth and its two subsystems, atmosphere and land-ocean, for 1850–2021.

Secondly, we compute the second derivative by time of the system's delay time, which indicates that Earth experienced a major change in its dynamics in the past by exhibiting a turning point which is when the deacceleration rate of the system's delay time goes through a maximum, some time between 1925 and 1945. After

* Corresponding author.
E-mail address: jonas@iiasa.ac.at (M. Jonas).

https://doi.org/10.1016/j.scitotenv.2025.179922
Received 21 March 2025; Received in revised form 2 June 2025; Accepted 12 June 2025
Available online 27 June 2025

passing through the maximum, Earth's land-ocean subsystem does not respond characteristically to stress anymore; that is, outside its natural regime.

This finding suggests that the Earth system is on a slow end-of-life path since then, not necessarily collapsing as a whole; but, nonetheless, that it is becoming increasingly vulnerable to sub-global, threshold-transgressing incidents acting bottom-up which may cause the entire atmosphere–land and ocean system to ultimately collapse.

1. Introduction

Humans are destroying nature at an increasing rate, resulting in an unprecedented loss of the very life support systems upon which they depend (Steffen et al., 2004, 2015; WWF, 2018; Zalasiewicz et al., 2024). The need for international action is rising, with calls for global stewardship beyond national jurisdiction to safeguard critical biophysical systems that regulate resilience and state, and therefore livability, on Earth (WWF, 2018; Stoddard et al., 2021; Rockström et al., 2024).

Here we further the understanding of the planetary burden and its dynamics caused by the effect of the continued increase in greenhouse gas (GHG) emissions and by global warming from the rheological (stress–strain) perspective, building on the first attempt of Jonas et al. (2022). That is, we perceive the emission of anthropogenic GHGs, notably carbon (CO_2) from fossil fuel burning and land use, into the atmosphere as a stressor. This perspective goes beyond the global carbon mass balance perspective applied by the carbon community, which is widely referred to as the gold standard in assessing whether Earth will remain hospitable for life (Friedlingstein et al., 2022). There, the condition of Earth is surveyed in units of gigatons of carbon per year ($GtC\,yr^{-1}$), while we survey its condition in stress–strain units (stress in units of Pa, strain in units of 1) – allowing access to and insight into novel and important characteristics reflecting Earth's rheological status. That is, we apply the principles of rheology – meant to study the response of materials to stress – at planetary scales. The two characteristics in focus here are the stress power exerted by humans upon Earth and the second derivative by time of Earth's delay time, which allows us to draw conclusions regarding Earth's characteristic response to stress.

We note that – although the focus is on the atmosphere–land and ocean carbon system – the stress–strain approach described herein should not be considered an appendix to a mass-balance-based carbon cycle model. Instead, it leads to a self-standing model belonging to the suite of reduced models (such as radiation transfer, energy balance, or box-type carbon cycle models), which offer great benefits in safeguarding complex three-dimensional climate and global change models because they do not compromise complexity in principle. A stress–strain model is missing in that suite of support models. Here we advance the applicability and efficacy of such a model in an Earth systems context.

In their rheological (stress–strain) analysis of Earth's atmosphere–-land and ocean carbon system presented by Jonas et al. in 2022, the authors explore the idea of applying a Maxwell body (MB) consisting of elastic and damping (viscous) elements to reflect the overall behavior of that system in response to the uninterrupted increase in cumulative CO_2 emissions between 1850 and 2015, referred to as stress by us; while making use of the GCB 2016, the global carbon budget available at the time (Le Quéré et al., 2016), as one data source among others (with the consequence that the data processing applied now and then differ substantially; as explained in Section 4).

From the standpoint of a global observer, the CO_2 concentration in the atmosphere is increasing (rather quickly). Concomitantly, the atmosphere is warming (here combining the effect of tropospheric warming resulting also from GHG emissions other than those of CO_2 and stratospheric cooling) and expanding (by approximately 20–50 m and potentially more in the troposphere per decade since around 1980), while some of the carbon is being locked away (rather slowly) in land and oceans, likewise under the influence of global warming (Borsche et al., 2007; Lackner et al., 2011; Philipona et al., 2018; Steiner et al., 2011, 2020; Meng et al., 2021; Friedlingstein et al., 2022). We refer to these two processes together, the expansion of the atmosphere by volume and the uptake of carbon by sinks, as the overall strain response of the atmosphere–land and ocean carbon system. To an observer it is the overall strain response of that system that is unknown.

Here we advance the underlying rheological data set from an accuracy-consistency point of view by making use exclusively of the now available GCB 2022 (Friedlingstein et al., 2022). The advancements, which we realize herein, range widely but can all be assigned to improved data and data processing and strengthened model (MB) application.

Our study goes beyond these advancements. We address two important issues neither of which have been mentioned previously nor elsewhere. Firstly, we quantify stress power exerted by humans upon Earth and its two subsystems, atmosphere and land-ocean, for 1850–2021. Stress power (in $Pa\,yr^{-1}$) specifies the energy input per volume per year. For a balanced Earth not exposed to human-induced global warming, stress power centers around zero. Thus, the question to be answered is how stress power has developed over time until today?

Secondly, we compute the first and second derivatives by time of the system's delay time. In particular, the second derivative is sensitive to changes in the dynamics of the global atmosphere–land and ocean carbon system and allows these to be uncovered. Thus, the question arises what the deeper understanding of this systems knowledge is? We show that Earth experienced a change in its dynamics in the past. The second derivative exhibits a turning point which is when the deacceleration rate of the system's delay time goes through an extremum (maximum), some time between 1925 and 1945.

The historical change in Earth's dynamics should be interpreted prudently as critical. After passing through the maximum, we suspect that Earth's land-ocean subsystem does not, from then on, respond characteristically to stress anymore; that is, outside its natural regime. In the post-maximum phase, the land-ocean subsystem appears merely to be dragged along due to the uninterrupted increase in stress.

This finding suggests that, from a rheological perspective, Earth is on a slow end-of-life path since then, not necessarily collapsing as a whole; but, nonetheless, that it is becoming increasingly vulnerable to sub-global, threshold-transgressing incidents acting bottom-up which may cause the entire atmosphere–land and ocean system to ultimately collapse (Barnorsky et al., 2012; Lenton et al., 2023; Ripple et al., 2024; Wunderling et al., 2024). Our stress–strain approach can be understood as pointing at a systemic limit for real Earth if it becomes less resilient, e.g., if its heterogeneous distribution of sinks becomes less pronounced, i.e. more homogenous.

From a stress perspective, the uptake of both terrestrial and oceanic carbon is believed to have weakened over time (e.g., Azar and Johansson, 2022; Gruber et al., 2023; Sharma et al., 2023; Pan et al., 2024). The GCB 2022 data indicate that their uptake ratio behaves astonishingly linear for 1850–2021; however, leaving room for a slight deviation from linear to be considered. The data suggest that, over time, the uptake of oceanic carbon has weakened more than the uptake of terrestrial carbon. Our stress–strain model is flexible against this uncertainty. It is controlled by the global uptake of carbon and not by how the global uptake splits up into its land and ocean parts.

We recall our rheological model approach (MB), and its advancements, methodologically in Section 2, while we provide a complete overview of the newly applied data and conversion factors in Section 3.

In Section 4 we describe in detail the improved data processing serving as a basis for a strengthened model application in Section 5, where we present our findings for key model quantities: stress, strain, stress power upon Earth and its atmosphere and land-ocean subsystems, the uptake of carbon by both land and ocean in relative terms, delay time and memory, and the first and second derivative of delay time T by time. We conclude by taking account of our main findings in Section 6.

2. Method

This section expands the theoretical basis for the rheological (stress–strain) analysis of Earth's atmosphere–land and ocean carbon system, first presented by Jonas et al. (2022). Therein the authors explore the idea of applying a Maxwell body (MB) consisting of elastic and damping (viscous) elements to reflect the overall behavior of that system in response to the uninterrupted increase in cumulative CO_2 emissions between 1850 and 2015.

Here we extend the usefulness of an MB as our preferred stress-strain model to derive stress power exerted by humans upon Earth and the second derivative by time of Earth's delay time between 1850 and 2021. We summarize the data needs of this endeavor subsequently (in Section 3), which can be satisfied exclusively by the GCB 2022, the now available global carbon budget (Friedlingstein et al., 2022). To this end, the GCB data must be processed for use in a stress-strain context (what we do in Section 4),

We refer to the uninterrupted increase in cumulative CO_2 emissions between 1850 and 2021 as stress; and to the two processes, the expansion of the atmosphere by volume and the uptake of CO_2 by sinks, as Earth's overall strain response. We do not know, due to lack of data, how reversible this response is. We do know, however, that the two processes are out of sync and that the slower process (uptake of carbon by sinks) remembers the influence of the faster one (expansion of the atmosphere by volume) which runs ahead. This global-scale memory – Earth's memory – was first quantified by Jonas et al. (2022).

It is critical to note that, as therein, the slow-to-fast temporal offset is also assumed in this study to hold, with the consequence that there is no need to disentangle the exchange of both thermal energy and carbon throughout the atmosphere–land and ocean system.

The MB is a logical choice of rheological model given the uninterrupted increase in cumulative CO_2 emissions since 1850 (see also Jonas et al., 2022). Its mathematical treatment is standard (see Supplement Information 1). The MB consists of an elastic element (its constant, traditionally denoted E for Young's modulus, is replaced by the compression modulus K) and a damping (viscous) element (the damping constant is denoted D) to capture the stress–strain behavior of the global atmosphere–land and ocean carbon system (see Fig. 1), including its hereditary behavior, and to simulate how humankind propelled that global-scale experiment historically.

In addition to knowing the system's compression and damping characteristics K and D, we assume the overall strain to be exponential or close to exponential. With this information, the stress–strain (σ–ε) equation describing the MB between time 0 and time t can be applied in the stress-explicit form,

$$\sigma(t) = \sigma(0)exp\left(-\frac{K}{D}t\right) + K\int_0^t \dot{\varepsilon}(\tau)exp\left(\frac{K}{D}(\tau - t)\right)d\tau, \tag{1a}$$

with $\sigma(0)$ and $\varepsilon(0)$ denoting initial conditions and a dot the derivative by time (Roylance, 2001; Kelly, 2013; Bertram and Glüge, 2017); and with the strain and its rate of change assumed (as commonly done in the context of natural systems) to behave exponentially:

$$\varepsilon(t) = exp(\alpha t) - 1 \tag{2}$$

$$\dot{\varepsilon}(t) = \alpha exp(\alpha t), \tag{3}$$

where $\alpha > 0$ is the exponential growth factor. (See Table SI1-1 in Supplement Information 1 for a compilation of assumptions and equations related to our use of the MB.) Thus, in the best case, we must determine at least three unknown parameters: D, K and α (what we do in a more robust way than Jonas et al. in 2022).

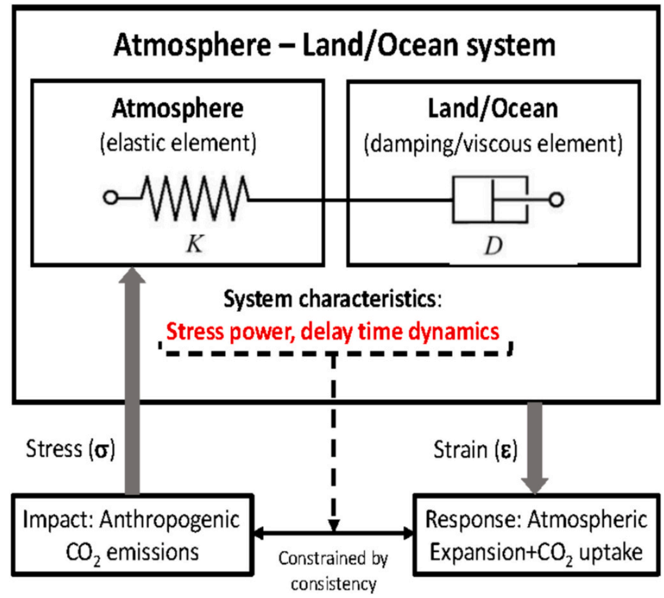

Fig. 1. Rheological model to capture the stress–strain behavior of the global atmosphere–land and ocean system as a Maxwell body (MB), consisting of elastic (atmosphere) and damping/viscous (land and ocean) elements. The stress (in units of Pa; known) is given by the carbon (CO_2) emissions from fossil fuel burning and land use, while the strain (in units of 1; assumed exponential, otherwise unknown) is given by the expansion of the atmosphere by volume and uptake of CO_2 by sinks. The model's three unknowns are K and D, the compression and damping characteristics of the MB, and α, the strain's exponential growth factor. The notion of consistency referred to in the figure does not include the negligible budget imbalance underlying the GCB 2022 (see Section 3). Source: Jonas et al. (2022: Fig. 1 adapted).

Ultimately, we assume initial conditions to be zero, or close to zero, in 1850. Thus, rewriting Eq. (1a) for $\sigma(0) = 0$ results in

$$\sigma(t) = \frac{D}{\beta}\dot{\varepsilon}(t)\left(1 - q_\beta^t\right) \tag{1b}$$

(see Eq. (2a) in Jonas et al., 2022), where $\beta = 1 + \frac{D}{K}\alpha$, $q = exp\left(-\frac{K}{D}\right)$ and $q_\beta = exp\left(-\frac{K}{D}\beta\right)$. To handle, in particular, bases and exponents properly in units of 1, we introduce the dimensionless time $n = \frac{t}{\Delta t}$ globally (where we refer to a temporal resolution of 1 year and set $\Delta t = 1yr$) such that, for example, $q^t = \left(exp\left(-\frac{K}{D}\Delta t\right)\right)^n$.

The CO_2-induced stress power (SP) exerted by humankind upon Earth as of 1850 is given by

$$SP = \sigma\dot{\varepsilon}, \tag{4}$$

and upon Earth's atmosphere (Atm) and land-ocean (LO) subsystems by

$$SP_K = SP - SP_D := SP_{Atm} \tag{5}$$

$$SP_D = \sigma\dot{\varepsilon}_D = \frac{\sigma^2}{D} := SP_{LO} \tag{6}$$

(see Bertram and Glüge, 2017), where ε_D is the part of the overall strain ε that can be assigned to the land and ocean carbon system (see Supplement Information 1).

Jonas et al. (2022) argue that the memory backward in time (here until 1850) of the atmosphere–land and ocean carbon system is captured by what they call the delay time

$$T(q,n) = \frac{q_\beta}{S_n}\left(\frac{\partial S_n}{\partial q_\beta}\right) = -\frac{q_\beta^n}{1-q_\beta^n}n + \frac{q_\beta}{1-q_\beta} \tag{7}$$

of the system (while α is held constant; see their Eq. 3, and Supplement Information 2), with $q_\beta = q_\alpha q$, $q_\alpha = exp(-\alpha\Delta t)$, and

$$S_n = S(q,n) = \frac{1-q_\beta^n}{1-q_\beta} := M(q,n) \tag{8}$$

quantifying the memory of the system. The first part of Eq. (7) suggests that T can also be interpreted as $\frac{\Delta M}{M}$ per $\frac{\Delta q}{q}$ which describes the (relative) change in memory per (relative) change in q if we would change q in retrospect at $n = 0$.

The first and second derivative of T by time are given by

$$\dot{T}(q,n) = \left\{-ln(q_\beta)\frac{q_\beta^n}{\left(1-q_\beta^n\right)^2}n - \frac{q_\beta^n}{1-q_\beta^n}\right\}yr^{-1} \tag{9}$$

(see Supplement Information 3); and

$$\ddot{T}(q,n) = -ln(q_\beta)\frac{q_\beta^n}{\left(1-q_\beta^n\right)^2}\left\{ln(q_\beta)\left(1+2\frac{q_\beta^n}{1-q_\beta^n}\right)n + 2\right\}yr^{-2} \tag{10}$$

(see Supplement Information 4). In particular, the second derivative is sensitive to changes in the dynamics of the global atmosphere–land and ocean carbon system and allows these changes to be uncovered.

We quantify Earth's viscoelastic behavior in Section 5.

3. Data and conversion factors

The GCB 2022 serves as our exclusive data source (see Tab. SI5–1 in Supplement Information 5). Friedlingstein et al. (2022) provide independent estimates of five source / sink components of the global CO_2 budget (all in $GtCyr^{-1}$): (1) emissions from fossil fuel combustion and oxidation from all energy and industrial processes, including cement production and carbonation (E_{FOS}); (2) emissions resulting from activities related to land use and land land-use change (E_{LUC}); (3) the growth rate of the CO_2 concentration in the atmosphere (G_{ATM}); and the uptake of CO_2 by both (4) oceans (S_{OCEAN}) and (5) land (S_{LAND}); and balance these globally by introducing B_{IM}

$$B_{IM} = E_{FOS} + E_{LUC} - (G_{ATM} + S_{OCEAN} + S_{LAND}), \tag{11}$$

a budget imbalance (see their Eq. (1)). B_{IM} is a measure of the mismatch between the estimated emissions and the estimated changes in the atmosphere, land, and ocean (Friedlingstein et al., 2022: Introduction). In their Section 3.8.2 the authors note that (with the focus on the period 1960–2021) B_{IM} is small and shows no trend, while it shows substantial variability on interannual to semi-decadal timescales. The cause of the variability in B_{IM} cannot be attributed. The authors assume errors in S_{LAND} and S_{OCEAN} to be the likely cause for the budget imbalance.

We do not account for B_{IM} for three reasons: (1) Our ultimate focus is on longer timescales (1850–1950 and 1850–2021, respectively), suggesting that B_{IM} is negligible. (2) The uptake of terrestrial and oceanic carbon is reflected by D, the damping constant in the stress–strain analogue, which comes with considerable uncertainty, large enough to overshadow B_{IM} (see Sections 4.1 to 4.3). (3) At the level of individual uptake of land (L) and ocean (O), reflected by D_L and D_O in the stress–strain analogue, we work with the (areally adjusted) ratio $\frac{D_L}{D_O}$ versus D which behaves astonishingly linearly (see Fig. 4 in Sections 4.1 and 5), indicating that the dynamics in the uptake of both terrestrial and oceanic carbon had developed in parallel (including their potential weakening) since 1850; in other words, virtually unaffected by variability. That is, working with the ratio $\frac{D_L}{D_O}$ allows the variability issue to be disregarded.

Table SI5-2 in Supplement Information 5 provides an overview of the carbon conversion and Earth surface factors that we use in our study. For reasons of conformance, the factors used by Friedlingstein et al. (2022: Table 1) to convert from gC to gCO_2 and from $ppmv\ CO_2$ to PgC are also used by us. In addition to Friedlingstein et al., we also consider the conversion from $ppmv\ CO_2$ to Pa as well as the fractional cover of the Earth surface by land and water.

4. Data processing

As stated in Section 2, we apply the MB in the stress-explicit mode. We use Eq. (1) to reproduce the stress $\sigma(t)$ which is known, given by the cumulative carbon (CO_2) emissions from fossil fuel burning and land use (converted to Pa). To start with, we assume the overall strain $\varepsilon(t)$ to be exponential, which leaves us with the problem of determining three unknown parameters: the compression and damping characteristics K and D of the MB, and the growth rate α of the strain.

In essence, our data processing aims at pre-selecting a skillful (min-max) range for D, defined by the validity of the MB. To this end, we derive rough estimates of $\lambda\left(=\frac{K}{D}\right)$ and α. These two parameters are determined quickly and sufficiently well – they pull the stress in different directions during its reproduction. Thereupon, K is calculated via λ. Finally, the pre-selected (min-max) range for D is narrowed down with the help of the monitored efficacy in determining λ and α. The three unknowns, including their uncertainties, are thus determined. It is their fine-tuned values which we then use to study Earth's atmosphere–land and ocean carbon system in greater depth than so far; viz. the human-induced stress power SP upon Earth and its subsystems, and the changes in its dynamics with the help of the first and second derivatives of delay time T by time (Section 5).

The data processing part consists of three steps: determining a gross range for D (Section 4.1); determining a narrow range for D (Section 4.2); and testing for an overall strain ε which is linear-exponential (Section 4.3) rather than exponential as in Sections 4.1 and 4.2. Several critical questions arise during the data processing which we address at the end of each (sub-) section. The differences as to how data are processed in both this study and Jonas et al. (2022) are subject of discussion in Section 4.1 and are recapitulated in Section 4.4.

4.1. Determining a gross range for global damping

This step consists of two parts:

A. Deriving the damping for land and ocean, D_L and D_O (thus, D) proportionally in scale. This we do for up to seven overlapping intervals across 1750–2021 by making use of the S_{LAND} and S_{OCEAN} data contained in the GCB 2022. And
B. identifying the appropriate order of magnitude for the proportionally-in-scale D values identified afore. This we do by multiplying the proportionally-in-scale D values with the same power-of-ten factor and performing stress-explicit experiments (as

Table 1
Breakdown of 1750–2021 into 7 intervals (see Supplement Data 2).

	Interval	Center	Span w/o center	Overlap with previous interval
	yr	*yr*	*yr*	*yr*
1.	1750–1900	1825	150	
2.	1850–1950	1900	100	51
3.	1925–1975	1950	50	26
4.	1955–1995	1975	40	21
5.	1985–2015	2000	30	11
6.	2004–2016	2010	12	12
7.	2009–2021	2015	12	8

described above) to derive estimates of λ and α.

To A:

We have been guided by the visual inspection of both

- the sum of annual emissions from fossil fuel combustion and oxidation (including cement production and carbonation) and those resulting from activities related to land use and land-use change (in *GtC*), $FF + Cem + LU$ in our notation (see Fig. 2a and Supplement Data 1); and
- the sum of these, but cumulated, emissions (in *Pa*), termed stress in our terminology (see Fig. 2b and Supplement Data 1); to identify a temporal breakdown of overlapping intervals across 1750–2021 (see Table 1 and Supplement Data 2):

For each of these intervals we proceed as described by Jonas et al. (2022) in their Sections 4.1 and 4.2, the idea being that we distill D_L and D_O from S_{LAND} and S_{OCEAN} following a standardized procedure, which ensures that D_L and D_O are correct in terms of both physical units and quantitatively relative to each other (though not yet necessarily in the right order of magnitude): We plot $\frac{\Delta S_i}{S_i}$ against time – where i denotes L (land) or O (ocean), S_i is referenced to pre-industrial conditions pertaining to land and ocean (see Canadell et al., 2021: Fig. 5.12), and ΔS_i measures deviations from S_i – which allows rates of strain (in yr^{-1}) to be derived. A linear fit works well in either case (see Fig. 3a,b). Thereupon, plotting annual changes in atmospheric CO_2 (in *ppmv*), normalized on the aforementioned rates of strain, versus time allows the remaining trends to be interpreted, by interval, as average damping constants for land and ocean (in *Pa yr* upon converting *ppmv* to *Pa*). Their appropriate uncertainty is given by half the maximal range (see Supplement Data 3 and 4).

Finally, the damping constant for a mean Earth is derived by multiplying the proportionally-in-scale damping constants for land (D_L)

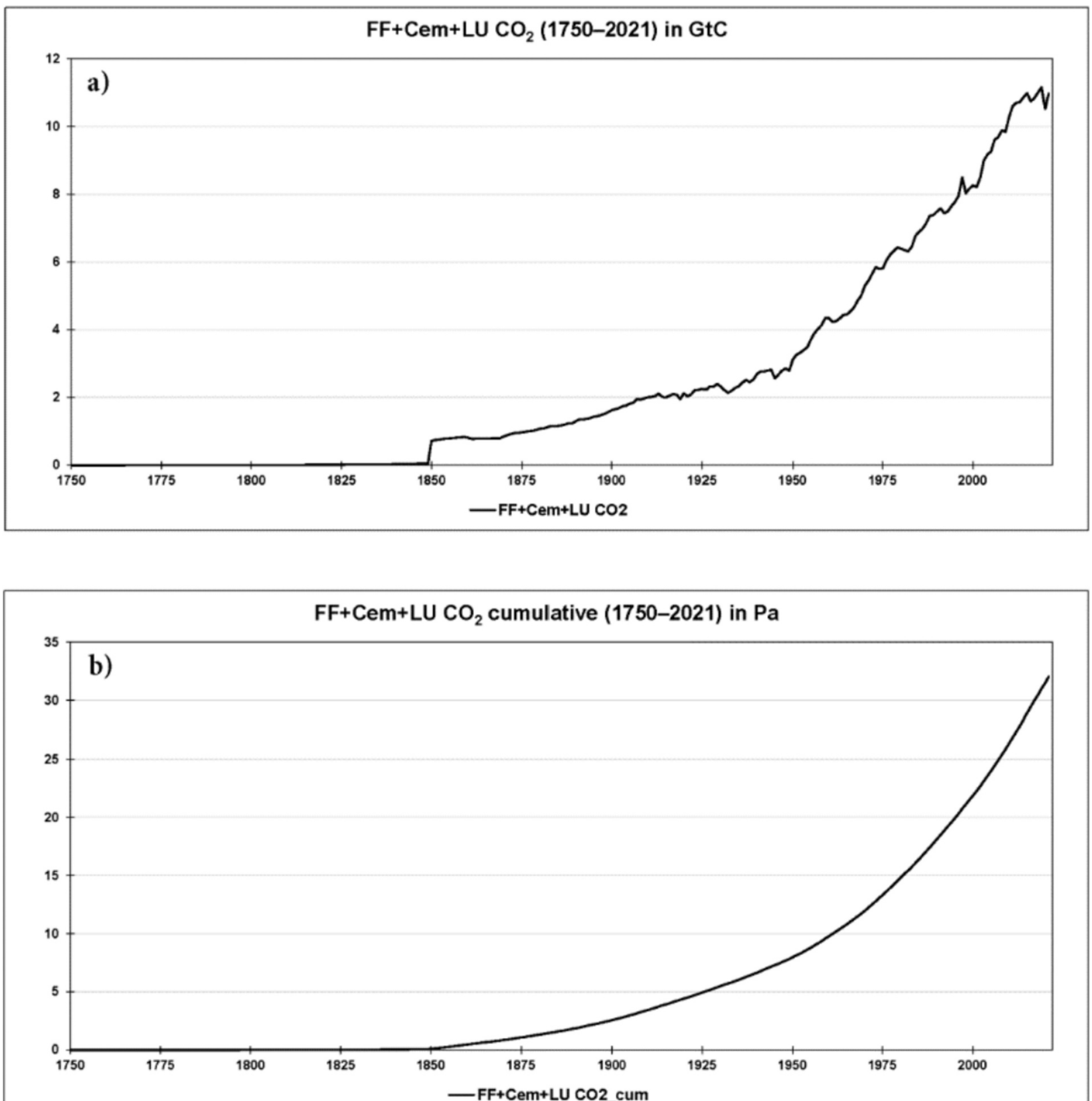

Fig. 2. a) Annual CO_2 emissions from fossil fuel combustion and oxidation, cement production and carbonation, and those resulting from activities related to land use and land land-use change (in *GtC*) for 1750–2021 ($FF + Cem + LU$ in our notation). b) CO_2 emissions as in Fig. 2a but cumulated (in *Pa*) for 1750–2021 (stress in our terminology). Source: Supplement Data 1.

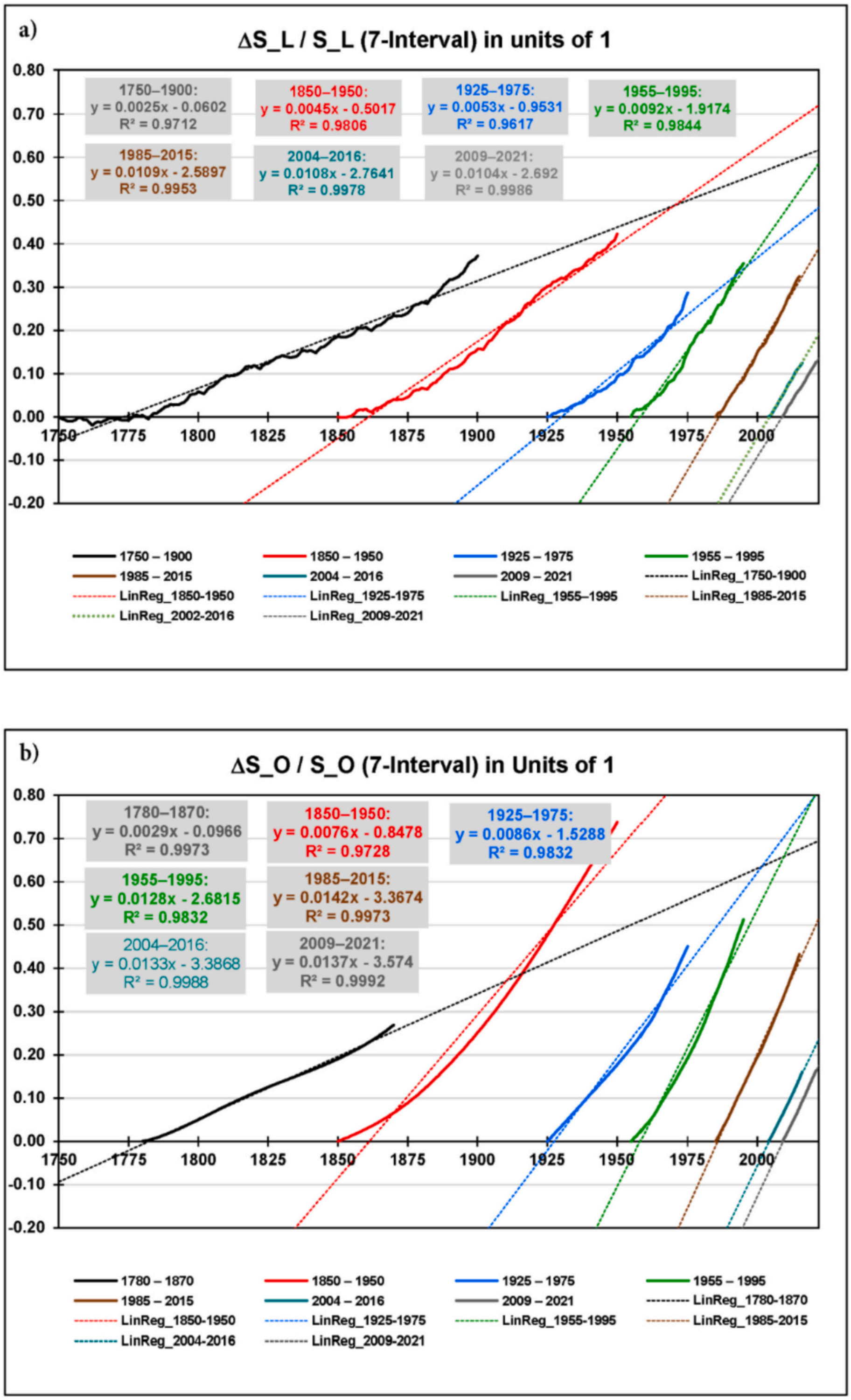

Fig. 3. a) $\frac{\Delta S_L}{S_L}$ and b) $\frac{\Delta S_O}{S_O}$ versus time across 7 intervals, where L and O denote land and ocean, S_L and S_O are referenced to pre-industrial conditions pertaining to land and ocean (see Canadell et al., 2021: Fig. 5.12), and ΔS_L and ΔS_O measure deviations from S_L and S_O, respectively. The slopes of the linear fits allow rates of strain (in yr^{-1}) to be derived. Source: Supplement Data 3 and 4.

and ocean (D_O) with Earth's fractional cover of land ($\frac{F_L}{F}$) and ocean ($\frac{F_O}{F}$), respectively:

$$\frac{F_L}{F}D_L + \frac{F_O}{F}D_O = D \tag{12}$$

(see Table 2 and Fig. 4 summarizing Supplement Data 5). We know that, in the case of a paralclel connection, stress adds up: $\sigma = \sigma_1 + \sigma_2$, where stress is measured in $Pa = \frac{N}{m^2}$ (force per square meter), and σ_1 and σ_2 refer to one and the same square meter areally. However, D_L and D_O do not do this; they refer to square meter of land and square meter of ocean, respectively. Multiplying D_L and D_O with $\frac{F_L}{F}$ and $\frac{F_O}{F}$ makes both refer to square meter of Earth. Jonas et al. (2022) did not apply this areal correction at the time; however, globally, the impact on the results is limited (see Section 4.4).

We note that our multi-interval approach applied in this section runs counter to the notion of constant viscoelastic parameters that are valid throughout; that is, across all intervals. In the course of our study, we will reduce the uncertainty surrounding D (see last column in Table 2) by about a factor 2, which allows D to be interpreted as a constant with appropriate uncertainty. The application of an MB will not be impaired by this magnitude of uncertainty.

To B:

So far, we know the ranges proportional in scale for D_L and D_O (thus, D), but not yet their order of magnitude. Jonas et al.'s 2022 estimate of D is (387 ± 74) *Pa yr* suggesting that, although still to be reassessed in this study, a proportionality factor is still missing.

To this end we conduct a series of numerical experiments with the sole purpose of testing the validity of our MB, not yet its optimized application. We multiply the proportionally-in-scale D values with the same power-of-ten factor and test whether stress-explicit experiments can be performed to derive estimates of λ and α, as described at the beginning of Section 4. To do so and proceed across intervals $(t_0 \leq t_1 \leq t)$, we adapt Eq. (1a) accordingly to

$$\sigma(t) = \sigma(t_1)exp\left(\frac{K}{D}(t_1 - t)\right) + \frac{D}{\beta}\alpha exp(\alpha t)\left(1 - exp\left(\frac{K}{D}\beta(t_1 - t)\right)\right) \quad (1c)$$

(see Supplement Information 6). Table SI7-1 in Supplement Information 7 summarizes our experiments carried out in Supplement Data 6–12 and recapped in Supplement Data 13 and 14. We find that

- a multiplication factor of 10^2 to increase the proportionally-in-scale D values prior to applying Eq. (1c) works well for all intervals except for the first (1750–1900); while the multiplication factor applied to the proportionally-in-scale D value of the first interval (10^0) does not work for the other intervals (see column 1750–1900 and rows 3–8 in Tab. SI7-1). The reason is that the emission data are consistent only as of 1850 which is when LU emissions kick in as an important part of the stressor (opposite to CEM, cement production and carbonation, as of 1931; see Fig. 2a), causing the stress to resemble the bended hockey-stick shape in Fig. 2b. Fig. 5a,b show the strongly differing results of the reproduced stress for 1750–1900 for $D = 4.148$ *Pa yr* and $D = 414.8$ *Pa yr* (see column 1750–1900 in Tab. SI7-1 for the respective parameter sets). We therefore excluded the first interval from further data processing.
- 1850 (with $\sigma(1850) = 0.081$ *Pa*; see Supplement Data 7), instead of 1847 (with $\sigma(1847) = 0$ *Pa*), can be safely used as the start year for anthropogenic stress (due to $FF + LU$ at the time); that is, for the bended part of the hockey stick (see below). The parameters α, λ, and K agree closely, while the match between reported and reproduced stress is high. We capture the latter with the help of the sum of squares of differences (see column 1850–1950 in Tab. SI7-1). Supplement Data 6–12 allow the respective correlation coefficients for all intervals to be calculated as well. However, we consider these to be somewhat less amenable from the perspective of use as monitoring parameter under high-agreement conditions. Finally, 1847 as start year results from describing stress reported for 1850–2021 slightly backward in time (i.e., for the bended part of the hockey

Table 2
Proportionally-in-scale damping constants for land (D_L) and ocean (D_O) by interval. They are multiplied with Earth's fractional cover of land ($\frac{F_L}{F}$) and ocean ($\frac{F_O}{F}$) to derive the damping constant (D) for a mean Earth (see Supplement Data 5).

	Interval *yr*	Center *yr*	D_L *Pa yr*	D_O *Pa yr*	D *Pa yr*
1.	1750–1900	1825	5.3 ± 4.2	3.7 ± 1.8[a]	4.1 ± 1.8
2.	1850–1950	1900	5.7 ± 2.5	3.4 ± 1.5	4.0 ± 1.3
3.	1925–1975	1950	9.8 ± 8.8	6.0 ± 5.4	7.1 ± 4.6
4.	1955–1995	1975	13.0 ± 6.1	9.3 ± 4.4	10.4 ± 3.6
5.	1985–2015	2000	17.1 ± 4.7	13.1 ± 3.6	14.3 ± 2.9
6.	2004–2016	2010	20.7 ± 4.1	16.8 ± 3.3	18.0 ± 2.6
7.	2009–2021	2015	23.3 ± 1.6	17.7 ± 1.2	19.3 ± 1.0

[a] The first interval for D_O is 1780–1870 (with 1825 as its center). D_O for 1780–1870 is used as a proxy for 1750–1900 (also with 1825 as its center).

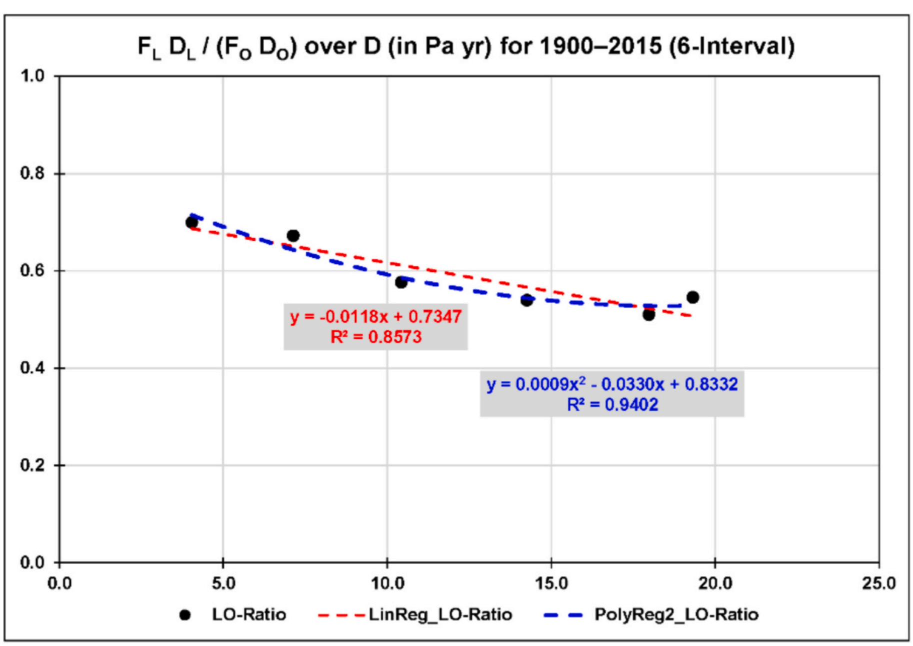

Fig. 4. Ratio of the proportionally-in-scale damping constants D_L and D_O, multiplied with Earth's fractional cover of land ($\frac{F_L}{F}$) and ocean ($\frac{F_O}{F}$), versus D, the damping constant reflecting a mean Earth (s. also Table 2). The values for the first interval (1750–1900) are not included (as justified in Section 4.1.B). Two trendlines are shown for the values of the remaining six intervals – a linear regression and a 2nd-order polynomial (which are further processed in Section 5). Source: Supplement Data 5.

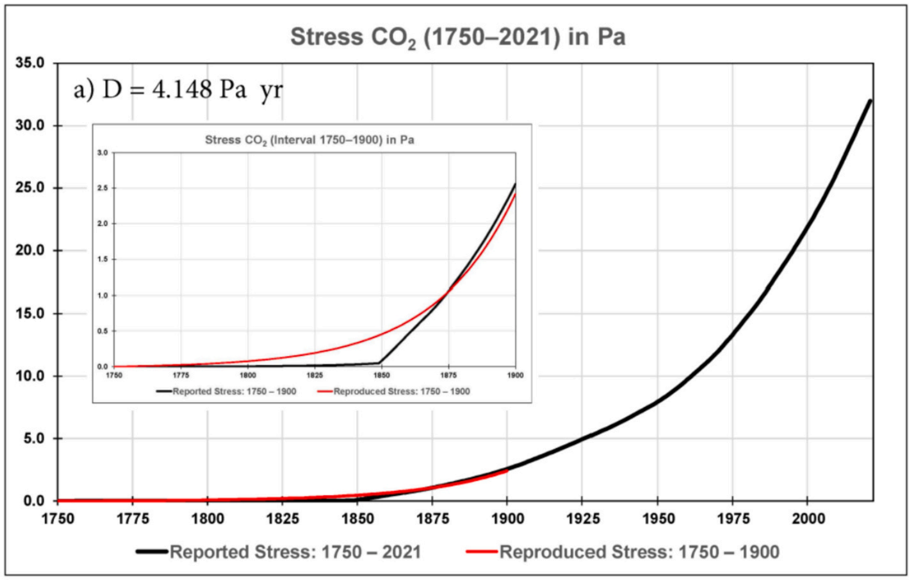

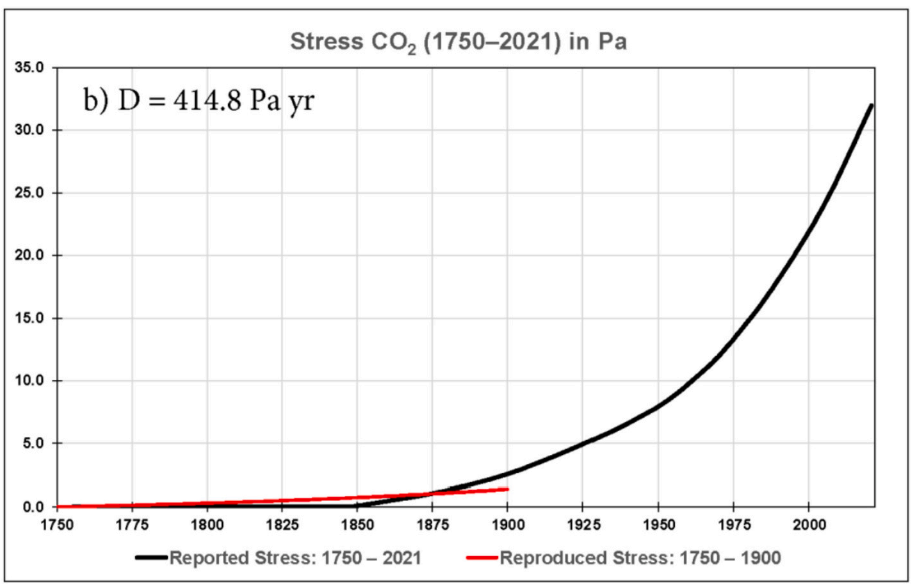

Fig. 5. a) Stress reported for 1750–2021 and reproduced for 1750–1900 (first interval) with the help of Eq. (1c) and $D = 4.148$ *Pa yr* (multiplication factor: 10^0; see also column 1750–1900 in Tab. SI7-1). The insert magnifies the misfit due to the sudden kick-in of LU emissions as of 1850. b) Stress reported for 1750–2021 and reproduced for 1750–1900 (first interval) with the help of Eq. (1c) and $D = 414.8$ *Pa yr* (multiplication factor: 10^2; see also column 1750–1900 in Tab. SI7-1), indicating the inapplicability of the MB for the selected *D* value. Source: Supplement Data 6.

stick) by means of a polynomial of order 4, an appropriate means for the given purpose only (see Supplement Data 7 and 13 and Fig. 6).

- the search for the appropriate order of magnitude of *D* (factor 10^2) outstrips by far the spread in the tuning parameters λ and α (factor $3-4$ and $1-2$, respectively; see rows 9–14, columns 1850–1950 onward, in Tab. SI7-1), resulting from a shift in the exponential function for the rate of strain. These robustness experiments we realized by setting $exp(\alpha t_1) = 1$, equivalent to setting $t_1 = t_0 = 0$ at the beginning of each interval, in the second term on the right side of Equation (SI6–1). That is, we deliberately assumed the rate of strain to phase-in exponentially anew at the beginning of each interval (which is how Jonas et al. proceeded in Jonas et al., 2022). This procedure does not obstruct the search for the gross range for *D* in principle.

Table SI7-2 in Supplement Information 7 summarizes additional numerical experiments carried out subsequently to those listed in Table SI7-1 (see Supplement Data 15–21). These experiments encompass one two-interval (1850–1950 and 1950–2021) and two one-interval experiments (1850–2021 and 1750–2021) for a power-of-ten factor of 2 and for $t_1 = t_0 = 0$ at the beginning of each interval globally (that is, $exp(\alpha t_1) = 1$ in the second term on the right side of Equation (SI6–1)). In particular, the three experiments 1850–1950, 1850–2021, and 1750–2021 with the starting point fixed at 1850 or 1750, respectively, lead us to conjecture that a narrow range for *D* should be expected below 600 to 700 *Pa yr* rather than above (see rows 1–4 in Tab. SI7-2). For that specific reason only, we re-introduced the first interval (1750–1900), that is, stress data prior to 1850 irrespective of their inhomogeneity. Fig. SI7-1a and SI7-1b in Supplement Information 7 show the match between reported and reproduced stress for 1850–2021 and 1750–2021 (see columns 1850–2021 and 1750–2021 in Tab. SI7-2).

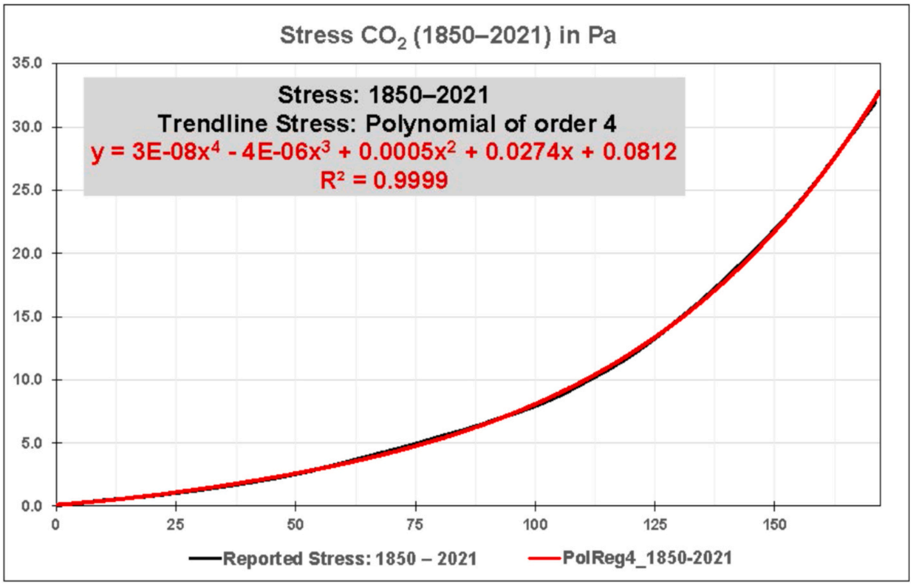

Fig. 6. Stress reported for 1850–2021 (scaled to 0–171 in the figure) and reproduced with the help of a polynomial of order 4 (see parameter insert). The polynomial is used for determining the onset of anthropogenic stress after excluding *FF* and *LU* emissions for 1750–1849. With $\sigma = 0.004\ Pa$ the onset is assigned to 1847 (see also column 1850–1950 in Tab. SI7-1). Source: Supplement Data 7.

4.2. Determining a narrow range for global damping

In this step we conduct a series of numerical experiments with the purpose of narrowing down the range for D. The experiments are of prognostic nature in retrospect and are stricter than those conducted under Section 4.1, while we keep the starting point for anthropogenic stress fixed at 1850 (with $\sigma(1850) = 0.081\ Pa$). We reproduce the stress $\sigma(t)$ for 1850–1950 and 1850–2021 in combination (simultaneous experiments) for $t_1 = t_0 = 0$ in 1850, while we require increasingly strict quality targets to be reached: The combined (total) sum of squares of differences, as mentioned an indicator for the quality of the match between reported and reproduced stress, is reduced from 4.2 to 4.0 to 3.9 Pa^2. These quality values are arbitrary; they are based on our multi-experimental experience and can be considered a good compromise between the quality of both the match and the approximation of $\lambda\left(=\frac{K}{D}\right)$ and α beyond discernible limits (see below). Running experiments for D ranging from 100 to 800 $Pa\,yr$ (see Supplement Data 22–34), it becomes visible that only for a subset of D, viz. $D \in [150; 600]\ Pa\,yr$, these targets can be reached at least partly. In the experiments we increased D in steps of 50 $Pa\,yr$ from 150 to 500 $Pa\,yr$, and in a single step of 100 $Pa\,yr$ from 500 to 600 $Pa\,yr$ (see Supplement Data 35 and Tab. SI8–1 in Supplement Information 8).

For a given D value, both λ and α are varied until the combined (total) sum of squares of differences becomes as small as the selected target. The respective values of λ and α then serve as reference tuple against which sensitivity tests are conducted as follows: Either λ or α are now varied beyond discernible limits, viz. by one unit in their sixth digit so that the total sum of squares of differences falls below or above of that of the reference tuple. If the unit changes in the sixth digit are too coarse, λ and α are varied by one unit in their seventh digit (equivalent to a decrease in sensitivity). The spread (intervals) in the total sums of squares of differences serves as an indicator for the efficacy of reaching the preselected quality target. To combine intervals, the sum-in-quadrature rule is applied.

We find that $D \in]150; 600[\ Pa\,yr$ satisfies the 4.2 Pa^2 quality target; $D \in [200; 500[\ Pa\,yr$ the 4.0 Pa^2 quality target; and $D \in [200; 450[\ Pa\,yr$ the 3.9 Pa^2 quality target. To this end, we choose $[200; 400]\ Pa\,yr$ as our best range for D; and $D = 250\ Pa\,yr$ as our best estimate within that range because it discloses the greatest sensitivity with respect to, thus potential for, further reductions in the total sum of squares of differences (see Supplement Data 35 and Tab. SI8–1).

Table 3 provides an overview of parameters and their values for $D \in [200; 400]\ Pa\,yr$, in addition to those for λ and α (see Tab. SI8–2 in Supplement Information 8 for a more comprehensive overview). Further reductions in the total sum of squares of differences result in negligible changes in the parameter values only.

4.3. Linear-exponential strain

In this step we test for a conceivable deviation from a purely exponential strain (see Eqs. (2) and (3)). To allow for a stark deviation, we consider a linear contribution. Two approaches are immediately obvious to expand the intrinsic behavior of the strain from exponential to linear-exponential. The first approach considers a linear-exponential contribution, in addition to a purely exponential one, in the rate of strain:

$$\dot{\varepsilon}(t) = \alpha(1 + mt)exp(\alpha t), \tag{13}$$

while the second approach considers a linear-exponential contribution, in addition to a purely exponential one, in the strain instead of its rate:

$$\varepsilon(t) = (1 + mt)exp(\alpha t) - 1; \tag{14}$$

with m in yr^{-1}. The stress-explicit equations under the initial-value assumption $\sigma(0) = 0$ are

$$\sigma(t) = m\frac{\alpha}{\beta}Dtexp(\alpha t) + \frac{\alpha}{\beta}D\left(1 - m\frac{1}{\beta}\frac{D}{K}\right)exp(\alpha t)\left(1 - q_\beta^t\right) \tag{15}$$

and

$$\sigma(t) = m\frac{\alpha}{\beta}Dtexp(\alpha t) + \frac{\alpha}{\beta}D\left(1 - m\left(\frac{1}{\beta}\frac{D}{K} - \frac{1}{\alpha}\right)\right)exp(\alpha t)\left(1 - q_\beta^t\right), \tag{16}$$

respectively (see Supplement Information 9 and 10). The two equations differ in the second, the purely exponential term only, which for a given $\sigma(t)$ and nearly equal-size D, K and α is greater in Eq. (16) than its pendant in Eq. (15); with the consequence that its first, the linear-exponential term is smaller (due to a smaller m) in Eq. (16) than its

Table 3
Narrow range for D arising from the combined (simultaneous) experiments for 1850–1950 and 1850–2021 and acknowledging the quality target of 3.9 Pa^2: Overview of key parameters and their values, in addition to those for α and λ (see Supplement Data 36).

Type of experiment: prognostic in retrospect (1850–1950 and 1850–2021) Sum of squares of differences: 3.90 Pa^2		D				
		200	250	300	350	400
		$Pa\,yr$	$Pa\,yr$	$Pa\,yr$	$Pa\,yr$	$Pa\,yr$
α	yr^{-1}	0.0190	0.0187	0.0186	0.0184	0.0181
$\lambda\,(=K/D)$	yr^{-1}	0.0097	0.0074	0.0061	0.0052	0.0047
$K = D^*\lambda$	Pa	1.93	1.86	1.83	1.81	1.87
$\beta = 1 + \alpha\,(D/K)$	1	2.96	3.52	4.05	4.56	4.88
$\lambda_\beta = (K/D)^*\beta = (K/D) + \alpha$	yr^{-1}	0.0286	0.0262	0.0246	0.0236	0.0228
$q_\beta = exp(-\lambda_\beta{}^*1yr)$	1	0.9718	0.9742	0.9757	0.9767	0.9775
$T_\infty = q_\beta/\left(1-q_\beta\right)$	1	34.4	37.7	40.1	41.9	43.4
$M_\infty = T_\infty/q_\beta$	1	35.4	38.7	41.1	42.9	44.4

pendant in Eq. (15).

However, we prefer using Eq. (15) over Eq. (16) for another reason. We consider the expansion of Eq. (3) by Eq. (13) more consistent from a rheological, an MB, perspective rather than the expansion of Eq. (2) by Eq. (14).

Our numerical experiments in this step build on those in Section 4.2, viz. for $D = 200$, 250, and 400 $Pa\,yr$, in particular; while we keep λ (thus, K) fixed. We, therefore, preserve the MB as rheological model. We vary α and m only.

Table SI11-1 in Supplement Information 11 summarizes our numerical experiments (see Supplement Data 37–39). They follow up our experiments under Section 4.2 which satisfy the 3.9 Pa^2 quality target (see Tab. SI8–1c in Supplement Information 8).

The outcome of our experiments is unambiguous. We find that

- the linear-exponential contribution of Eq. (15) is negligible with respect to both m (see $m \neq 0$ values in column 6 in Table SI11-1) and the change in the total sum of squares of differences (see values pertinent to $m = 0$ and $m \neq 0$ in column 7 in Tab. SI11–1). The m value is even lowest for our best estimate $D = 250$ $Pa\,yr$. The impact of the linear-exponential contribution on the total sum of squares of differences is comparable to changes caused by adjusting the stress so that for $t_1 = t_0 = 0$ in 1850 $\sigma(t_1) = 0.0$ Pa (instead of $\sigma(t_1) = 0.081$ Pa) (see values in column 4 and, pertinent to $m = 0$, column 7 in Tab. SI11–1).
- considering a linear-exponential contribution does not necessarily lead to a reduction (improvement) in the total sum of squares of differences (quality target) (see values for $D = 400$ $Pa\,yr$ in column 4 and, pertinent to $m = 0$, column 7 in Tab. SI11–1).

We, therefore, conclude that our assumption of the strain behaving exponentially is justified.

4.4. Data processing: recap of advancements

We complete Section 4 by recapitulating the advanced data processing applied in this study compared to how Jonas et al. proceeded in 2022. As mentioned before, the advancements would not have been possible without the authors' 2022 analysis.

An important strength of the 2022 study, concomitantly a weakness, was the use of data in addition to those of the GCB 2016 (see Jonas et al., 2022: Tab. SI6–1). So did the authors use, with reference to 1959–2015, both net primary productivity and photosynthetic data for determining D_L and dissolved inorganic carbon data for determining D_O. The individual estimates for $D_L \approx (83 \pm 44)$ $Pa\,yr$ and $D_O \approx (304 \pm 60)$ $Pa\,yr$ were combined without areal correction to $D \approx (387 \pm 74)$ $Pa\,yr$. However (and correctly), multiplying D_L and D_O with Earth's fractional cover of land ($\frac{F_L}{F}$) and ocean ($\frac{F_O}{F}$) gives $D \approx 239$ $Pa\,yr$, which agrees astonishingly well with our best estimate of $D \approx 250$ $Pa\,yr$. Even the respective uncertainty ranges overlap considerably: $[313; 461]$ $Pa\,yr$ then versus $[200; 400]$ $Pa\,yr$ now.

By way of contrast, an important weakness was the authors' estimate of $K \approx (100 \pm 90)$ Pa at the time. Guided by the distribution of atmospheric mass by altitude, they chose the stratopause as the top of the atmosphere (at about 48 km altitude and 100 Pa), with uncertainty ranging from mid-to-higher stratosphere (at about 43 km altitude and 190 Pa) to mid-mesosphere (at about 65 km altitude and 10 Pa). However, this estimate can be easily off track because atmospheric mass by altitude scales exponentially. We now derive K in the order of about $\sim$ 2 Pa (see Table 3), a factor of five smaller than even the authors' lower estimate of K then.

The underestimate of K, in combination with the authors' choice of letting the rate of strain phase-in exponentially anew (i.e., in 1959) in their 1959–2015 experiments (see also Section 4.1.B), are the reason why the study of Jonas et al. (2022) can be compared qualitatively with our initial data processing work under Section 4.1, where we aimed at determining the gross range for D.

Table 4 justifies this qualitative statement. The table shows that the experiments of Jonas et al. (2022) and ours with start year 1850 agree remarkably well despite the differences in the D values. The differences are stipulated by the respective experimental set-ups and are compensated for by the differences, equal in size in relative terms, in the values of α and K (see rows 5, 7 and 9 in Table 4). This comparison further underscores the value of the earlier results achieved by Jonas et al. for this study. Note that the serial experimental set-up (1850–1958 followed by 1959–2015) applied by the authors at the time is of no relevance here.

5. Main findings

Here we report on our findings resulting from our strictest experiments conducted under Section 4.2. These experiments are of prognostic nature in retrospect; that is, for 1850–1950 and 1850–2021 in combination (simultaneous experiments) with $t_1 = t_0 = 0$ in 1850 and the starting point for anthropogenic stress kept fixed at 1850 (with $\sigma(1850) = 0.081$ Pa, unless indicated otherwise). Our findings refer to $D = 200$ and 400 $Pa\,yr$ to cover the range of D, and to $D = 250$ $Pa\,yr$ as our best estimate in that range. We recall that our stress-strain approach refers to a mean Earth.

5.1. Reproduced stress

As to be expected, for $D = 200$, 250 and 400 $Pa\,yr$, reproduced and reported stress match well (see Fig. SI12–1 in Supplement Information 12) because of the strict quality target (total sum of squares of differences) applied (3.9 Pa^2). Table 5 indicates that this target does not divide equally over the two intervals 1850–1950 and 1850–2021. In the case of $D = 250$ $Pa\,yr$, the sum of squares of differences is greatest for 1850–1950 but lowest for 1850–2021; that is, its predictive power (in

Table 4
Comparison of parameters for experiments with start year 1850: Experiment 1850–1958 conducted by Jonas et al. (2022: Tab. SI10-2) and two experiments conducted in this study under Section 4.1.B (1850–1950) and Section 4.2 (1850–1950 in combination with 1850–2021). In addition to the temporal match, the D value is used as additional reference for the comparison. Thus, the 1850–1958 experiment with $D = 467.9$ $Pa\,yr$ is matched most closely by both the 1850–1950 experiment with $D = 403.4$ $Pa\,yr$ and the 1850–1950/2021 experiment with $D = 400$ $Pa\,yr$.

Interval		1850–1958	1850–1950	1850–1950 and 1850–2021
Source		Jonas et al. (2022)	This study	
		Tab. SI10–2	Tab. SI7-1 and Supplement Data 7	Table 3
Parameter	Unit	$t_1 = 0$ @ 1850	$t_1 = 0$ @ 1850 and $t_1 = 3$ @ 1850	$t_1 = 0$ @ 1850
D	$Pa\,yr$	467.9	403.4	400
$\sigma(1850)$	Pa	0	0.081	0.081
α	yr^{-1}	0.0151	0.0179–0.0180	0.0181
$\lambda\ (= K/D)$	yr^{-1}	0.0045	0.0045–0.0047	0.0047
$K = D^*\lambda$	Pa	2.1	1.8–1.9	1.9
$\beta = 1 + \alpha\,(D/K)$	1	4.4	4.8–5.0	4.9
$\lambda_\beta = (K/D)^*\beta = (K/D) + \alpha$	yr^{-1}	0.0196	0.0224–0.0227	0.0228
$q_\beta = exp(-\lambda_\beta{}^*1yr)$	1	0.9806	0.9776–0.9779	0.9775
$T_\infty = q_\beta/\left(1 - q_\beta\right)$	1	50.6	43.6–44.2	43.4
$M_\infty = T_\infty/q_\beta$	1	51.6	44.6–45.2	44.4
Sum of squares of differences	Pa^2	1.10	0.66	3.90

Table 5
Match between reproduced and reported emissions: Sums of squares of differences by interval, 1850–1950 versus 1850–2021 (see Supplement Data 24, 27 and 30).

D	Sum of squares of differences (Pa^2)		
$Pa\,yr$	1850–1950	1850–2021	Combined
200	0.9851	2.9149	3.90
250	1.1022	2.7981	3.90
400	0.7199	3.1804	3.90

retrospect) is greatest although the match between reproduced and reported stress is equal to that for $D = 200$ and 400 $Pa\,yr$.

5.2. Strain and stress power

We use Eqs. (2) and (4) to calculate both strain and stress power as of 1850 (see Fig. 7 and 8 and Supplement Data 40). The latter requires the input of stress which, as we already know, can be well reproduced by a polynomial of order 4 (see Fig. 6 and insert therein).

However, instead of $\sigma(1850) = 0.081$ Pa, we now request $\sigma(1850) = 0$ Pa to allow strain to start from zero in 1850. To check whether this request comes with implications, we construct the fourth-order polynomial for the reported stress, an appropriate means for the given purpose only. We find that the polynomial is virtually identical, within the number of digits displayed, to the one mentioned in Fig. 6, but now without the constant term on the right side, yet still with $R^2 = 0.9999$ (see Supplement Data 40). However, while emphasizing this polynomial match, we note that the polynomials' coefficients do not agree in their higher-order digits, and we also recall that we consider correlation coefficients less amenable than sums of squares of differences to monitor high-agreement conditions (see Section 4.1.B).

We use Eqs. (5) and (6) to break down stress power further into those parts, which act upon Earth's atmosphere (Atm) and land-ocean (LO) subsystems (see Fig. 9 and Supplement Data 41). As to be expected, stress power diversifies for the LO subsystem, while virtually not at all for the atmosphere.

5.3. Damping land versus damping oceans

To split D into its parts D_L and D_O, we start from the linear regression displayed in Fig. 4

$$\left(\frac{F_L}{F_O}\frac{D_L}{D_O}\right) = -0.0118\frac{1}{Pa\,yr}D + 0.7347, \tag{17a}$$

which we assume to be valid in principle, that is, across scales; and which we can therefore extend, here to proportional-in-scale values of D ranging between 2 and 4 $Pa\,yr$. We consider the extension of the range of validity for D an auxiliary means, allowing Eq. (17a) to be adapted (here by 10^2) to adjust D conveniently to its right order of magnitude:

$$\left(\frac{F_L}{F_O}\frac{D_L}{D_O}\right) = -\frac{0.0118}{100}\frac{1}{Pa\,yr}(100\,D) + 0.7347. \tag{17b}$$

We use Eq. (17b) to determine for any $D \in [200; 400]$ $Pa\,yr$ the ratio $\frac{F_L}{F_O}\frac{D_L}{D_O}$ which allows all its parts, in combination with Eq. (12), to be derived (see Table 6 and Supplement Data 42). This procedure also holds if the $\left(\frac{F_L}{F_O}\frac{D_L}{D_O}\right) - D$ relationship is captured by the second-order polynomial also displayed in Fig. 4 (see also Table 6).

Both the linear and the second-order polynomial regressions indicate that $\frac{F_L}{F_O}\frac{D_L}{D_O}$ decreases when D increases. An increase in D is equivalent to a continuous weakening of the combined land-ocean carbon sink; while a decrease in the ratio $\frac{F_L}{F_O}\frac{D_L}{D_O}$ suggests that, with both the numerator and the denominator increasing concomitantly, the ocean sink weakens faster than the terrestrial sink.

5.4. Delay time and memory

We use Eqs. (7) and (8) to derive delay time T and memory M for 1850–2021 and beyond by perpetuating long-term historical conditions until 2100 (see Fig. 10 and Supplement Data 43). The increase of both T and M with time is limited as shown in the figure. Their respective limits are given in Table 3 and their 2021 levels relative to these limits in Table 7.

As Fig. 10 shows both T and M increase with increasing D. This can be explained by an uptake of carbon that happens more slowly over time, and which exerts an influence reaching further back in time.

5.5. First and second derivative of delay time by time.

We use Eqs. (9) and (10) to derive the first and second derivative of delay time T by time for 1850–2021 and beyond by perpetuating long-term historical conditions until 2100 (see Fig. 11). The second derivative is noteworthy. It exhibits a distinct turning point when the deceleration rate of the system's delay time goes through a maximum (see Fig. 12). We determine the maximum by constructing the year-to-year difference of the 2nd derivative of delay time; a procedure which we consider approximate (we deal with small numbers) yet still sufficiently effective (see Supplement Data 43). The turning point lies between 1925

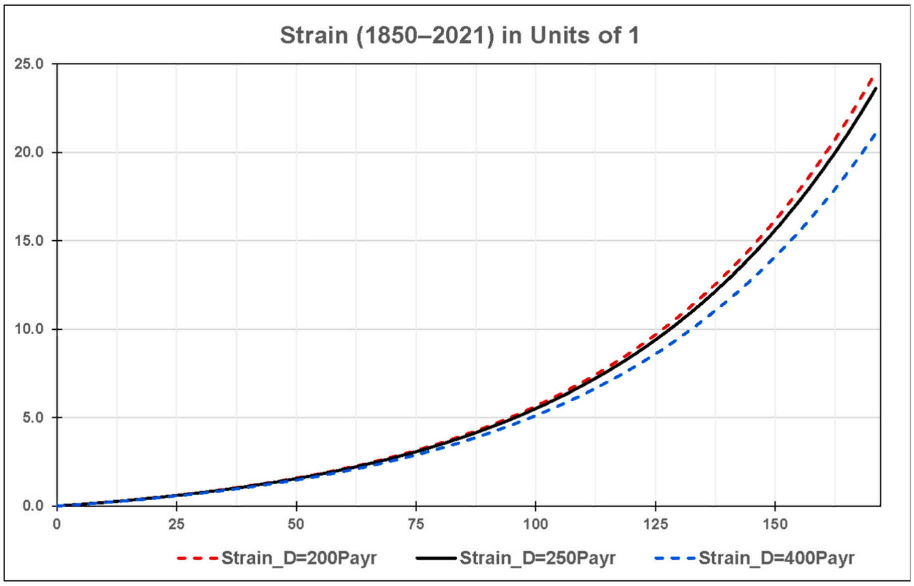

Fig. 7. Strain for 1850–2021 (scaled to 0–171 in the figure) according to Eq. (2) for $D = 200$, 250 and 400 $Pa\,yr$ (with $\sigma(1850) = 0\,Pa$). Source: Supplement Data 40.

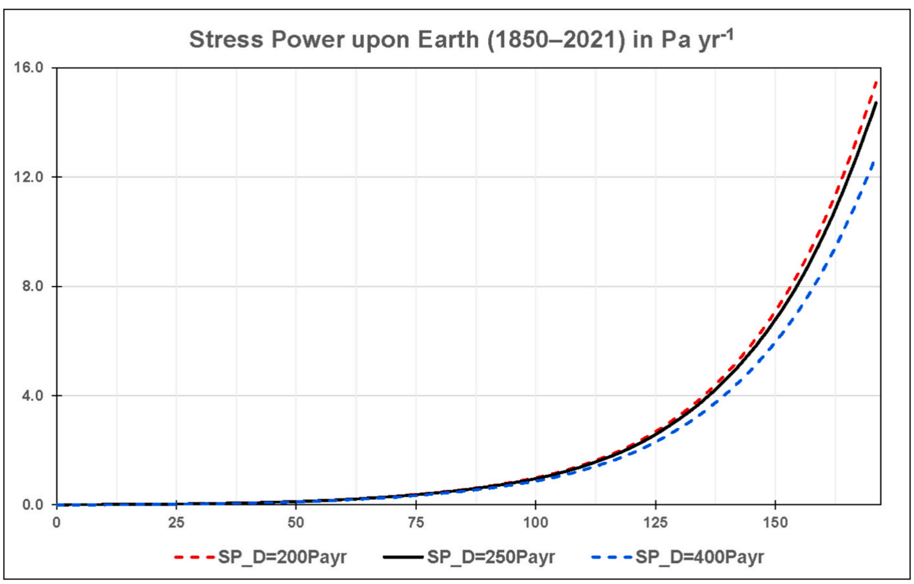

Fig. 8. Stress power (SP) upon Earth for 1850–2021 (scaled to 0–171 in the figure) according to Eq. (4) for $D = 200$, 250 and 400 $Pa\,yr$ (with $\sigma(1850) = 0\,Pa$). Source: Supplement Data 40.

and 1945, dependent on D (see Fig. 12): at 1925 (or 75 in year-equivalent units) for $D = 200\,Pa\,yr$, 1932 (or 82 in year-equivalent units) for $D = 250\,Pa\,yr$, and 1945 (or 95 in year-equivalent units) for $D = 400\,Pa\,yr$.

Table 8 summarizes values of key quantities – stress, strain, stress power upon Earth and its atmosphere and land-ocean subsystems – for $D = 200$, 250 and 400 $Pa\,yr$ in the year of turning point (1925, 1932, and 1945) and, for comparison, in year 2021.

6. Account of findings

Our study advances the rheological (stress–strain) analysis of Earth's atmosphere–land and ocean carbon system. The stress upon Earth is given by the cumulative CO_2 emissions from fossil fuel burning and oxidation (including cement production and carbonation) and those resulting from activities related to land use and land-use change; while the two processes, the expansion of the atmosphere by volume and the uptake of CO_2 by sinks, are referred to as Earth's overall strain response. We do not know, due to lack of data, how reversible this response is. We do know, however, that the two processes are out of sync and that the slower process (uptake of carbon by sinks) remembers the influence of the faster one (expansion of the atmosphere by volume) which runs ahead. The MB is a logical choice of stress–strain model to study the ramifications of the uninterrupted increase in cumulative atmospheric CO_2 emissions upon sinks, including hereditary behavior, for 1850–2021 and beyond.

We do not disentangle the exchange of both thermal energy and carbon throughout the atmosphere–land and ocean system. That is, we assume that the slow-to-fast temporal offset between slowly and quickly reacting subsystems is (sufficiently) stable and holds; an assumption that still requires to be corroborated thoroughly. We value the additional degree of reductionism, whilst preserving complexity, as an invaluable

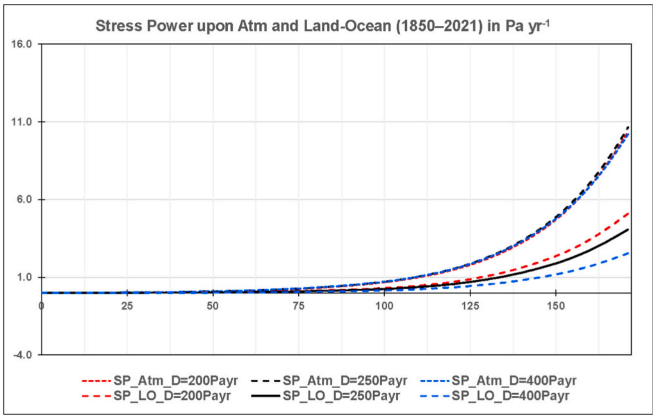

Fig. 9. Stress power (SP) upon Earth's atmosphere (Atm) and land-ocean (LO) subsystems for 1850–2021 (scaled to 0–171 in the figure) according to Eqs. (5) and (6) for $D = 200$, 250 and 400 *Pa yr* (with $\sigma(1850) = 0$ *Pa*). Source: Supplement Data 41.

Table 6
Split-up of D into D_L and D_O for $D = 200$, 250 and 400 *Pa yr*, making use of both the (linear and 2nd-order polynomial) regressions displayed in Fig. 4 and Eq. (12) (see Supplement Data 42).

D	$\frac{F_L}{F_O}\frac{D_L}{D_O}$	$\frac{F_L}{F}D_L$	$\frac{F_O}{F}D_O$	D_L	D_O
Pa yr	1	*Pa yr*	*Pa yr*	*Pa yr*	*Pa yr*
Linear regression: $y = -0.0118\,x + 0.7347$					
200	0.711	83	117	284	165
250	0.705	103	147	353	207
400	0.687	163	237	556	335
2nd-order polynomial regression: $y = 0.0009\,x^2 - 0.033\,x + 0.8332$					
200	0.771	87	113	297	160
250	0.756	108	142	367	201
400	0.715	167	233	569	330

advantage in studying Earth's strain response in greater depth.

Although the focus is on the atmosphere–land and ocean carbon system, it is called to mind that the stress–strain approach described herein should not be considered an appendix to a mass-balance-based carbon cycle model. Instead, it leads to a self-standing model belonging to the suite of reduced but still insightful models (such as radiation transfer, energy balance, or box-type carbon cycle models), which offer great benefits in safeguarding complex three-dimensional climate and global change models because they do not compromise complexity in principle. A stress-strain model was missing in that suite of support models – what does not come unexpectedly given that complex models do not integrate, to the best of our knowledge, a stress-strain perspective.

In our study, we make a great effort to advance the underlying rheological data from an accuracy-consistency point of view by making use exclusively of the now available GCB 2022. The advancements range widely but can all be assigned to improved data and data processing and strengthened model (MB) application.

It is the improved data which we then use to study Earth's atmosphere–land and ocean carbon system in greater depth than so far. We address two important issues that had neither been mentioned previously nor elsewhere. Firstly, we quantify stress power exerted by humans upon Earth and its two subsystems, atmosphere and land-ocean, for 1850–2021. Secondly, we explore whether the derivatives by time of the system's delay time are sensitive to changes in the dynamics of the global atmosphere–land and ocean carbon system and whether these changes can be uncovered.

To tackle the two challenges, we apply the MB in its stress-explicit version, where we assume Earth's overall strain to be exponential, an assumption which we scrutinize in part but do not question in principle. Experiments alternative to those carried out by Jonas et al. (2022) are conducted to gauge whether a more robust range for D can be identified, yet still on the basis of fitting reproduced and reported stress. In essence, and most importantly, in determining D Jonas et al. **(i)** used a serial

Table 7
2021 levels of T and M relative to their limiting values T_∞ and M_∞ for $D = 200$, 250 and 400 *Pa yr* (with $\sigma(1850) = 0.081$ *Pa*) (see Supplement Data 43).

D	$\frac{T}{T_\infty}$	$\frac{M}{M_\infty}$
Pa yr	%	%
200	96.3	99.3
250	94.8	98.9
400	91.8	98.0

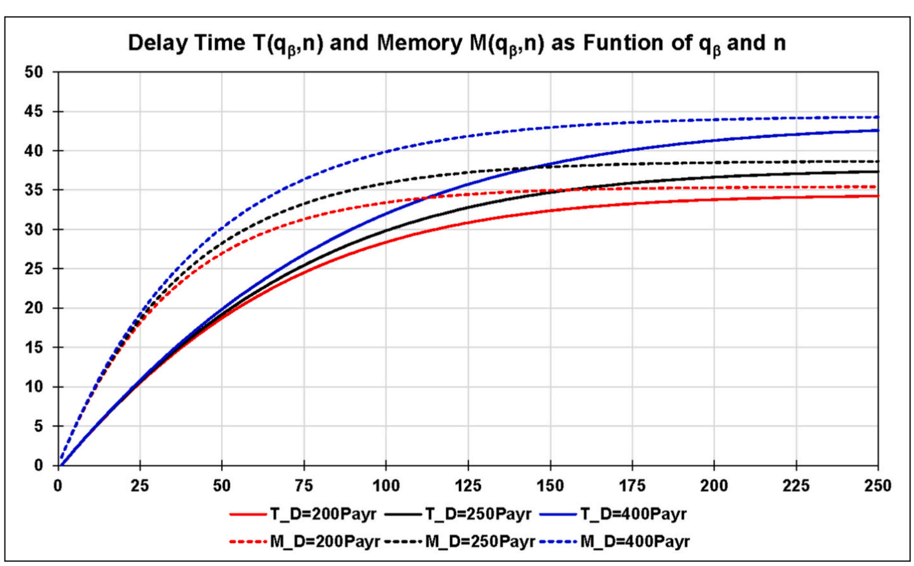

Fig. 10. Delay time T and memory M (in units of 1) for 1850–2100 (scaled to 0–250 in the figure) according to Eqs. (7) and (8) for $D = 200$, 250 and 400 *Pa yr* (with $\sigma(1850) = 0.081$ *Pa*). Source: Supplement Data 43.

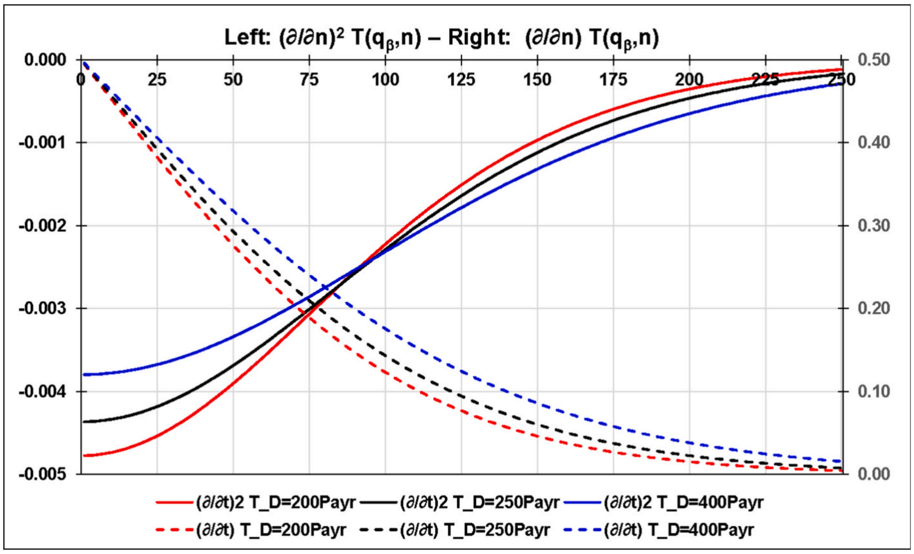

Fig. 11. First and second derivative of delay time T by time (in units of yr^{-1} and yr^{-2}, respectively) for 1850–2100 (scaled to 0–250 in the figure) according to Eqs. (9) and (10) for $D = 200$, 250 and 400 $Pa\,yr$ (with $\sigma(1850) = 0.081\,Pa$). Source: Supplement Data 43.

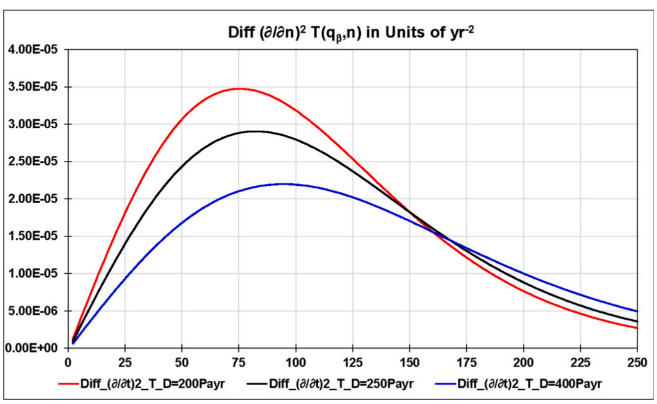

Fig. 12. Year-to-year difference (Diff) of the second derivative of delay time T by time (in units of yr^{-2}) in Fig. 11 to determine its maximum, which is in year-equivalent units at 75 (or 1925) for $D = 200\,Pa\,yr$, 82 (or 1932) for $D = 250\,Pa\,yr$, and 95 (or 1945) for $D = 400\,Pa\,yr$. Source: Supplement Data 43.

experimental setup (1850–1958 followed by 1959–2015), resulting in a two-model realization (that is, two MBs with not fundamentally differing viscoelastic parameters); and **(ii)** relied on K, the highly sensitive compression modulus. This we overcome by **(i)** using a parallel experimental setup (1850–1950 and 1850–2021 in combination); and **(ii)** varying both λ (the viscoelastic parameter ratio of the MB) and α (the exponential growth factor of the strain), while monitoring the efficacy of that fitting process to determine D independently of K. The compression modulus is derived only thereafter via λ.

It is the parameter triplet (D, λ, α) thus quantified – with $D \in [200; 400]\,Pa\,yr$, $\lambda \in [0.0047; 0.0097]\,yr^{-1}$, and $\alpha \in [0.0181; 0.0190]\,yr^{-1}$ (see Table 3) – which is consistent with a one-model realization throughout 1850–2021 and which is used, in long last, in tackling the aforementioned two challenges.

Prior to quantifying stress power for 1850–2021, we quantify strain, which we estimate to range globally between 21.1 and 24.6 (in units of 1) in 2021, dependent on D (see Table 8). Stress power (in $Pa\,yr^{-1}$) specifies the energy input per volume per year. We estimate stress power to range globally between 12.8 and 15.5 $Pa\,yr^{-1}$ in 2021; with the greater share, $10.2 - 10.6\,Pa\,yr^{-1}$, acting upon the atmosphere, and the smaller share, $2.5 - 5.1\,Pa\,yr^{-1}$, upon the land-ocean subsystem (see Table 8). For comparison, both strain and stress power center around zero for a balanced Earth not exposed to human-induced global warming.

Table 8
Values of key quantities for $D = 200$, 250 and 400 $Pa\,yr$ (with $\sigma(1850) = 0\,Pa$) in the year of turning point (TP) (1925, 1932, and 1945) and in year 2021: stress, strain, stress power upon Earth and its subsystems, atmosphere and land-ocean (see Supplement Data 40 and 41).

D	$Pa\,yr$	200	250	400
@ TP in		1925	1932	1945
σ reported	Pa	4.84	5.60	7.18
σ reproduced	Pa	4.69	5.47	7.33
ε	1	3.14	3.65	4.58
SP	$Pa\,yr^{-1}$	0.38	0.49	0.73
SP_{Atm}	$Pa\,yr^{-1}$	0.26	0.36	0.60
SP_{LO}	$Pa\,yr^{-1}$	0.12	0.13	0.13
in		2021	2021	2021
σ reported	Pa	31.91	31.91	31.91
σ reproduced	Pa	32.51	32.42	32.13
ε	1	24.57	23.62	21.10
SP	$Pa\,yr^{-1}$	15.47	14.72	12.76
SP_{Atm}	$Pa\,yr^{-1}$	10.37	10.65	10.22
SP_{LO}	$Pa\,yr^{-1}$	5.09	4.07	2.55
Ratio			2021 to TP	
σ reported	1	6.6	5.7	4.4
σ reproduced	1	6.9	5.9	4.4
ε	1	7.8	6.5	4.6
SP	1	40.6	30.2	17.6
SP_{Atm}	1	43.4	32.4	19.7
SP_{LO}	1	39.4	29.4	17.1

We find the second derivative by time of the system's delay time particularly informative as it allows changes in the dynamics of the global atmosphere–land and ocean carbon system to be uncovered. The second derivative exhibits a turning point which is when the deacceleration rate of the system's delay time goes through a maximum. The turning point lies between 1925 and 1945, dependent on D: at 1925 (or 75 in year-equivalent units) for $D = 200\,Pa\,yr$, 1932 (or 82 in year-equivalent units) for $D = 250\,Pa\,yr$, and 1945 (or 95 in year-equivalent units) for $D = 400\,Pa\,yr$ (see Fig. 12).

We consider our evaluation of the second temporal derivative of the system's delay time reliable. Hence, we are surprised ourselves by the emergence of the turning point so distinct and early in time. We suspect that this is because our stress-strain approach refers to a mean Earth whose sinks are distributed evenly across the globe. We speculate that real Earth with its unevenly distributed sinks is more resilient in that it also exhibits a turning point but later in time. We presume that our stress-strain approach points at a systemic limit for real Earth and its unevenly distributed sinks.

The change in Earth's dynamics should be interpreted prudently as critical. After passing through the maximum, we suspect that Earth's land-ocean subsystem does not, from then on, respond characteristically to stress anymore; that is, outside its natural regime. In the post-maximum phase, the land-ocean subsystem appears merely to be dragged along due to the uninterrupted increase in stress.

This lets us conjecture whether, from a rheological perspective, Earth is on a slow end-of-life path since then, not necessarily collapsing as a whole; but, nonetheless, whether it is becoming increasingly vulnerable to sub-global, threshold-transgressing incidents acting bottom-up which, if increasing in number or outreach, may cause the entire atmosphere–land and ocean system to ultimately collapse. The presumption that Earth is in an even worse environmental condition than commonly believed cannot be rejected.

Our rheological model, as presented hitherto, is unaffected of, but preserves, the land-ocean carbon sequestration inherent in the GCB 2022, i.e. the $\left(\frac{F_L}{F_O}\frac{D_L}{D_O}\right) - D$ relationship which appears to be linear or even polynomial of second-order (see Table 6). GCB's sink data, adjusted areally for their fractional cover globally, indicate that the carbon uptake of both land and ocean has weakened over time, the uptake of oceanic carbon more than the uptake of terrestrial carbon.

In conclusion, the challenge remains for researchers to disentangle the carbon uptake of both land and ocean more clearly, retrospectively as well as prospectively; and to decipher also more clearly, across spheres, the probability of threshold-transgressing incidents interacting and influencing each other. An increasing number of such incidents, or even their cascading, should be of extreme concern because, from a rheological perspective, we are approximating potentially disastrous mean-Earth conditions.

Supplementary data to this article can be found online at https://doi.org/10.1016/j.scitotenv.2025.179922.

CRediT authorship contribution statement

Matthias Jonas: Writing – review & editing, Writing – original draft, Visualization, Validation, Supervision, Software, Resources, Project administration, Methodology, Investigation, Formal analysis, Data curation, Conceptualization. **Rostyslav Bun:** Validation, Supervision, Methodology. **Iryna Ryzha:** Validation, Supervision. **Piotr Żebrowski:** Validation, Software.

Financial support

This research has been supported by the authors' home institutions, the International Institute for Applied Systems Analysis, and the Lviv Polytechnic National University.

Declaration of competing interest

The authors declare that they have no known competing financial interests or personal relationships that could have appeared to influence the work reported in this paper.

Acknowledgements

We are grateful to Ansa Heyl for editorial support and to the two anonymous reviewers for their valuable comments and remarks.

Appendix A. Acronyms and nomenclature

Atm	atmosphere (index)
B	budget (in $GtC\,yr^{-1}$)
C	carbon
CEM	emissions from cement production and carbonation (in *GtC*)
CO_2	carbon dioxide
D	damping constant (in *Pa yr*)
Diff	difference (in yr^{-2})
E	in the context of the GCB 2022: emissions (in $GtC\,yr^{-1}$)
E	in the context of the MB: Young's modulus (in *Pa*)
FF	emissions from fossil fuel combustion and oxidation (in *GtC*)
FOS	emissions from fossil fuel combustion and oxidation, including cement production and carbonation (index)
G	growth rate of the atmospheric CO_2 concentration (in $GtC\,yr^{-1}$)
GCB	global carbon budget
GHG	greenhouse gas
IM	imbalance (index)
K	compression modulus (in *Pa*)
L	in the context of the MB: land (index)
LAND	in the context of the GCB 2022: land (index)
LO	land-ocean (index)
LU	emissions from land use and land-use change (in *GtC*)
LUC	emissions from land use and land-use change (index)
M	memory (in units of 1)
MB	Maxwell body
n	dimensionless time (in units of 1)
O	ocean (index)
OCEAN	ocean (index)
q	auxiliary quantity (in units of 1)
S	sink (in $GtC\,yr^{-1}$)
SD	supplement data

SP	stress power (in $Pa\,yr^{-1}$)
SI	supplement information
t	time (in *yr* or dimensionless in units of 1)
T	delay time (in units of 1)
TP	turning point
α	exponential growth factor of the strain (in yr^{-1})
β	auxiliary quantity (in units of 1)
β	division by β (index)
ε	strain (in units of 1)
λ	auxiliary quantity (in yr^{-1})
σ	stress (in *Pa*)

Data availability

Our study is supported by a Supplement provided by the authors. It consists of two parts, (1) Supplement Information (SI) and (2) Supplement Data (SD). The two parts of the Supplement are available online at doi:https://doi.org/10.5281/zenodo.13944574 (Jonas et al., 2025).

References

Azar, C., Johansson, D.J.A., 2022. IPCC and the effectiveness of carbon sinks. Environ. Res. Lett. 17, 041004. https://iopscience.iop.org/article/10.1088/1748-9326/ac5bb2.

Barnorsky, A.D., Hadly, E.A., Bascompte, J., Berlow, E.L., Brown, J.H., Fortelius, M., Getz, W.M., Harte, J., Hastings, A., Marquet, P.A., Martinez, N.D., Mooers, A., Roopnarine, P., Vermeij, G., Williams, J.W., Gillespie, R., Kitzes, J., Marshall, C., Matzke, N., Mindell, D.P., Revilla, E., Smith, A.B., 2012. Approaching a state shift in Earth's biosphere. Nature 486, 52–58. https://doi.org/10.1038/nature11018.

Bertram, A., Glüge, R., 2017. Festkörpermechanik. Otto-von-Guericke University Magdeburg, Magdeburg, Germany. ISBN: 978-3-940961-88-4 (s. 1.3.2).

Borsche, M., Kirchengast, G., Foelsche, U., 2007. Tropical tropopause climatology as observed with radio occultation measurements from CHAMP compared to ECMWF and NCEP analyses. Geophys. Res. Lett. 34, L03702. https://agupubs.onlinelibrary.wiley.com/doi/10.1029/2006GL027918.

Canadell, J.G., Monteiro, P.M.S., Costa, M.H., Cotrim da Cunha, L., Cox, P.M., Eliseev, A. V., Henson, S., Ishii, M., Jaccard, S., Koven, C., Lohila, A., Patra, P.K., Piao, S., Rogelj, J., Syampungani, S., Zaehle, S., Zickfeld, K., 2021. Global carbon and other biogeochemical cycles and feedbacks. In Climate Change 2021. In: Masson-Delmotte, V., Zhai, P., Pirani, A., Connors, S.L., Péan, C., Berger, S., Caud, N., Chen, Y., Goldfarb, L., Gomis, M.I., Huang, M., Leitzell, K., Lonnoy, E., Matthews, J. B.R., Maycock, T.K., Waterfield, T., Yelekçi, O., Yu, R., Zhou, B. (Eds.), The Physical Science Basis. Contribution of Working Group I to the Sixth Assessment Report of the Intergovernmental Panel on Climate Change. Cambridge University Press, Cambridge, United Kingdom and New York, NY, USA, pp. 673–816. https://www.ipcc.ch/report/ar6/wg1/downloads/report/IPCC_AR6_WGI_Chapter05.pdf, 2021.

Friedlingstein, P., O'Sullivan, M., Jones, M.W., Andrew, R.M., Gregor, L., Hauck, J., Le Quéré, C., Luijkx, I.T., Olsen, A., Peters, G.P., Peters, W., Pongratz, J., Schwingshackl, C., Sitch, S., Canadell, J.G., Ciais, P., Jackson, R.B., Alin, S.R., Alkama, R., Arneth, A., Arora, V.K., Bates, N.R., Becker, M., Bellouin, N., Bittig, H.C., Bopp, L., Chevallier, F., Chini, L.P., Cronin, M., Evans, W., Falk, S., Feely, R.A., Gasser, T., Gehlen, M., Gkritzalis, T., Gloege, L., Grassi, G., Gruber, N., Gürses, Ö., Harris, I., Hefner, M., Houghton, R.A., Hurtt, G.C., Iida, Y., Ilyina, T., Jain, A.K., Jersild, A., Kadono, K., Kato, E., Kennedy, D., Klein Goldewijk, K., Knauer, J., Korsbakken, J.I., Landschützer, P., Lefèvre, N., Lindsay, K., Liu, J., Liu, Z., Marland, G., Mayot, N., McGrath, M.J., Metzl, N., Monacci, N.M., Munro, D.R., Nakaoka, S.-I., Niwa, Y., O'Brien, K., Ono, T., Palmer, P.I., Pan, N., Pierrot, D., Pocock, K., Poulter, B., Resplandy, L., Robertson, E., Rödenbeck, C., Rodriguez, C., Rosan, T.M., Schwinger, J., Séférian, R., Shutler, J.D., Skjelvan, I., Steinhoff, T., Sun, Q., Sutton, A.J., Sweeney, C., Takao, S., Tanhua, T., Tans, P.P., Tian, X., Tian, H., Tilbrook, B., Tsujino, H., Tubiello, F., van der Werf, G.R., Walker, A.P., Wanninkhof, R., Whitehead, C., Willstrand Wranne, A., Wright, R., Yuan, W., Yue, C., Yue, X., Zaehle, S., Zeng, J., Zheng, B., 2022. Global carbon budget 2022. Earth Syst. Sci. Data 14, 4811–4900. https://doi.org/10.5194/essd-14-4811-2022. https://www.icos-cp.eu/science-and-impact/global-carbon-budget/2022.

Gruber, N., Bakker, D.C.E., DeVries, T., Gregor, L., Hauck, J., Landschützer, P., McKinley, G.A., Müller, J.D., 2023. Trends and variability in the ocean carbon sink. Nat. Rev. Earth Environ. 4, 119–134. https://doi.org/10.1038/s43017-022-00381-x.

Jonas, M., Bun, R., Ryzha, I., Żebrowski, P., 2022. Quantifying memory and persistence in the atmosphere–land and ocean carbon system. ESD 13 (1), 439–455. https://doi.org/10.5194/esd-13-439-2022.

Jonas, M., Bun, R., Ryzha, I., Żebrowski, P., 2025. Supplement [consisting of supplement information and supplement data] to human-induced carbon stress power upon earth: integrated data set, rheological findings and consequences. IIASA. https://doi.org/10.5281/zenodo.13944574.

Kelly, P., 2013. Solid Mechanics Part I: an Introduction to Solid Mechanics. The University of Auckland, Auckland, NZ. https://pkel015.connect.amazon.auckland.ac.nz/SolidMechanicsBooks/Part_I/index.html (last access: 27 January 2025).

Lackner, B.C., Steiner, A.K., Hegerl, G.C., Kirchengast, G., 2011. Atmospheric climate change detection by radio occultation using a fingerprinting method. J. Climate 24, 5275–5291. https://doi.org/10.1175/2011JCLI3966.1.

Le Quéré, C., Andrew, R.M., Canadell, J.G., Sitch, S., Korsbakken, J.I., Peters, G.P., Manning, A.C., Boden, T.A., Tans, P.P., Houghton, R.A., Keeling, R.F., Alin, S., Andrews, O.D., Anthoni, P., Barbero, L., Bopp, L., Chevallier, F., Chini, L.P., Ciais, P., Currie, K., Delire, C., Doney, S.C., Friedlingstein, P., Gkritzalis, T., Harris, I., Hauck, J., Haverd, V., Hoppema, M., Klein Goldewijk, K., Jain, A.K., Kato, E., Körtzinger, A., Landschützer, P., Lefèvre, N., Lenton, A., Lienert, S., Lombardozzi, D., Melton, J.R., Metzl, N., Millero, F., Monteiro, P.M.S., Munro, D.R., Nabel, J.E.M.S., Nakaoka, S., O'Brien, K., Olsen, A., Omar, A.M., Ono, T., Pierrot, D., Poulter, B., Rödenbeck, C., Salisbury, J., Schuster, U., Schwinger, J., Séférian, R., Skjelvan, I., Stocker, B.D., Sutton, A.J., Takahashi, T., Tian, H., Tilbrook, B., van der Laan-Luijkx, I.T., van der Werf, G.R., Viovy, N., Walker, A.P., Wiltshire, A.J., Zaehle, S., 2016. Global carbon budget 2016. Earth Syst. Sci. Data 8, 605–649. https://doi.org/10.5194/essd-8-605-2016.

Lenton, T.M., Armstrong McKay, D.I., Loriani, S., Abrams, J.F., Lade, S.J., Donges, J.F., Milkoreit, M., Powell, T., Smith, S.R., Zimm, C., Buxton, J.E., Bailey, E., Laybourn, L., Ghadiali, A., Dyke, J.G., 2023. The Global Tipping Points Report 2023. University of Exeter, Exeter, UK. https://global-tipping-points.org/.

Meng, L., Liu, J., Tarasick, D.W., Randel, W.J., Steiner, A.K., Wilhelmsen, H., Wang, L., Haimberger, L., 2021. Continuous rise of the tropopause in the Northern Hemisphere over 1980–2020. Sci. Adv. 7 (45), eabi8065. https://www.science.org/doi/10.1126/sciadv.abi8065.

Pan, Y., Birdsey, R.A., Phillips, O.L., Houghton, R.A., Fang, J., Kauppi, P.E., Keith, H., Kurz, W.A., Ito, A., Lewis, S.L., Nabuurs, G.-J., Shvidenko, A., Hashimoto, S., Lerink, B., Schepaschenko, D., Castanho, A., Murdiyarso, D., 2024. The enduring world forest carbon sink. Nature 631, 563–569. https://doi.org/10.1038/s41586-024-07602-x.

Philipona, R., Mears, C., Fujiwara, M., Jeannet, P., Thorne, P., Bodeker, G., Haimberger, L., Hervo, M., Popp, C., Romanens, G., Steinbrecht, W., Stübi, R., Van Malderen, R., 2018. Radiosondes show that after decades of cooling, the lower stratosphere is now warming. J. Geophys. Res. Atmos. 123, 12509–12522. https://doi.org/10.1029/2018JD028901.

Ripple, W.J., Wolf, C., Gregg, J.W., Rockström, J., Mann, M.E., Oreskes, N., Lenton, T.M., Rahmstorf, S., Newsome, T.M., Xu, C., Svenning, J.-C., Pereira, C.C., Law, B.E., Crowther, T.W., 2024. The 2024 state of the climate report: perilous times on planet earth. BioScience, biae087. https://doi.org/10.1093/biosci/biae087.

Rockström, J., Kotze, L., Milutinović, S., Biermann, F., Brovkin, V., Donges, J., Ebbesson, J., French, D., Gupta, J., Kim, R., Lenton, T., Lenzi, D., Nakicenovic, N., Neumann, B., Schuppert, F., Winkelmann, R., Bosselmann, K., Folke, C., Lucht, W., Schlosber, D., Richradson, K., Steffen, W., 2024. The planetary commons: a new paradigm for safeguarding earth-regulating systems in the Anthropocene. Proc. Natl. Acad. Sci. 121 (5), e2301531121. https://doi.org/10.1073/pnas.2301531121.

Roylance, D., 2001. Engineering Viscoelasticity. Massachusetts Institute of Technology, Cambridge, MA, USA. http://web.mit.edu/course/3/3.11/www/modules/visco.pdf (last access: 27 January 2025), 24 October.

Sharma, B., Kumar, J., Ganguly, A.R., Hoffman, F.M., 2023. Carbon cycle extremes accelerate weakening of the land carbon sink in the late 21st century. BG 29, 1829–1841. https://doi.org/10.5194/bg-20-1829-2023.

Steffen, W., Sanderson, A., Tyson, P., Jäger, J., Matson, P., Moore III, B., Oldfield, F., Richardson, K., Schellnhuber, H.J., Turner II, B.L., Wasson, R.J., 2004. Global change and the Earth system: a planet under pressure. Springer-Verlag, Berlin, Germany, 978-3-540-26594-8,. http://www.igbp.net/publications/igbpbookseries/igbpbookseries/globalchangeandtheearthsystem2004.5.1b8ae20512db692f2a680007462.html.

Steffen, W., Richardson, K., Rockström, J., Cornell, S.E., Fetzer, I., Bennett, E.M., Biggs, R., Carpenter, S.R., de Vries, W., Wit, C.A., Folke, C., Gerten, D., Heinke, J., Mace, G.M., Persson, L.M., Ramanathan, V., Reyers, B., Sörlin, S., 2015. Planetary boundaries: guiding human development on a changing planet. Science 347 (6223), 1259855. https://doi.org/10.1126/science.1259855.

Steiner, A.K., Lackner, B.C., Ladstädter, F., Scherllin-Pirscher, B., Foelsche, U., Kirchengast, G., 2011. GPS radio occultation for climate monitoring and change detection. Radio Sci. 46, RS0D24. https://agupubs.onlinelibrary.wiley.com/doi/10.1029/2010RS004614.

Steiner, A.K., Ladstädter, F., Randel, W.J., Maycock, A.C., Fu, Q., Claud, C., Gleisner, H., Haimberger, L., Ho, S.-P., Keckhut, P., Leblanc, T., Mears, C., Polvani, L.M., Santer, B.D., Schmidt, T., Sofieva, V., Wing, R., Zou, C.-Z., 2020. Observed temperature changes in the troposphere and stratosphere from 1979 to 2018. J. Climate 33, 8165–8194. https://journals.ametsoc.org/view/journals/clim/33/19/jcliD190998.xml.

Stoddard, I., Anderson, K., Capstick, S., Carton, W., Depledge, J., Facer, K., Gough, C., Hache, F., Hoolohan, C., Hultman, M., Hällström, N., Kartha, S., Klinsky, S., Kuchler, M., Lövbrand, E., Nasiritousi, N., Newell, P., Peters, G.P., Sokona, Y., Stirling, A., Stilwell, M., Spash, C.L., Williams, M., 2021. Three decades of climate mitigation: why haven't we bent the global emissions curve? Annu. Rev. Environ. Resour. 46, 653. https://doi.org/10.1146/annurev-environ-012220-011104.

Wunderling, N., von der Heydt, A.S., Aksenov, Y., Barker, S., Bastiaansen, R., Brovkin, V., Brunetti, M., Couplet, V., Kleinen, T., Lear, C.H., Lohmann, J., Roman-Cuesta, R.M., Sinet, S., Swingedouw, D., Winkelmann, R., Anand, P., Barichivich, J., Bathiany, S., Baudena, M., Bruun, J.T., Chiessi, C.M., Coxall, H.K., Docquier, D., Donges, J.F., Falkena, S.K.J., Klose, A.K., Obura, D., Rocha, J., Rynders, S., Steinert, N.J., Willeit, M., 2024. Climate tipping point interactions and cascades: a review. Earth Syst. Dynam. 15, 41–74. https://doi.org/10.5194/esd-15-41-2024.

WWF, 2018. In: Grooten, M., Almond, R.E.A. (Eds.), Living planet report - 2018: aiming higher. WWF, Gland, Switzerland.

Zalasiewicz, J., Thomas, J.A., Waters, C.N., Turner, S., Head, M.J., 2024. What should the anthropoid mean? Nature 632, 980. https://www.nature.com/articles/d41586-024-02712-y.